Materials Horizons

ROYAL SOCIETY OF CHEMISTRY

REVIEW

View Article Online
View Journal | View Issue

Cite this: *Mater. Horiz.*, 2025, **12**, 5075

Side-chain engineering of conjugated molecules for n-type organic thermoelectrics†

Hangyang Li,[ab] Gang Ye,*[c] Yazhuo Kuang,[ab] Mingyu Ma,[ab] Shuyan Shao *[d] and Jian Liu *[ab]

Received 13th January 2025,
Accepted 15th April 2025

DOI: 10.1039/d5mh00067j

rsc.li/materials-horizons

The growing need for renewable energy sources has led to increased interest in organic thermoelectric (OTE) materials, which are mechanically flexible, cost-effective to process, and capable of converting thermal energy into electricity. Although p-type OTEs have shown promising efficiency, the development of n-type OTEs has not kept pace with their p-type counterparts in terms of performance, highlighting the need for additional research and innovation. This review outlines the basic principles and molecular design strategies for n-type OTEs. It then examines side-chain engineering in-depth, underscoring the complementary effects of backbone and side-chain modifications. Lastly, it discusses the challenges and future directions in developing n-type OTEs to inform the design strategies for these materials.

Wider impact

The side chains of conjugated macromolecules typically have insulating properties and do not conduct electrical charges. However, these side chains play a crucial role in solution-based processing, essential for the cost-effective and large-scale production of organic electronic devices. Side-chain engineering plays a vital role in influencing the performance of various electronic devices. This review summarizes recent advancements in the side-chain engineering of conjugated molecules specifically for n-type organic thermoelectrics. It explores how side chain characteristics—such as polarity, length, and spatial arrangement—affect molecular packing, charge carrier doping, intermolecular electrostatic forces, and overall thermoelectric efficiency. Particular attention is given to the role of ethylene glycol-like side chains. The insights from this review are applicable beyond organic thermoelectrics, providing valuable information for various electronic systems that utilize the doped configurations of conjugated molecules, including organic electrochemical transistors, electrochromic systems, and energy storage devices.

1. Introduction

Thermoelectric (TE) materials are used to directly convert thermal energy into electrical energy and have gained significant attention in recent years due to the increasing interest in renewable energy.[1–4] Organic thermoelectric (OTE) materials offer light weight,[5] flexibility,[6,7] low cost,[8] non-toxicity,[9] and easy and scalable fabrication,[10] with broad applications in energy harvesting,[11] temperature sensing,[12] solid-state cooling,[13] and portable and wearable electric generating devices.[14] In recent decades, substantial efforts have been made to enhance the performance of OTE materials and to gain a deeper understanding of their fundamental physical properties. This has also led to a better comprehension of the working principles and physical processes of OTE devices, triggering a new wave of research into OTE materials.

The fundamental principles that govern the performance of thermoelectric materials are based on the Seebeck effect.[15–17] This effect occurs when charge carriers move from the hot end of a material to the cold end. This movement creates an uneven distribution of charge carriers, which generates electricity in the form of a potential difference and an electric current within the material. The efficiency of thermoelectric materials is typically assessed using the dimensionless figure of merit (ZT). This evaluation involves three key parameters: the Seebeck coefficient (S), electrical conductivity (σ), and thermal conductivity (κ).

[a] *State Key Laboratory of Polymer Science and Technology, Changchun Institute of Applied Chemistry, Chinese Academy of Sciences, Changchun 130022, P. R. China. E-mail: jian.liu@ciac.ac.cn*
[b] *School of Applied Chemistry and Engineering, University of Science and Technology of China, Hefei 230026, P. R. China*
[c] *Key Laboratory for the Green Preparation and Application of Functional Materials, Hubei Key Laboratory of Polymer Materials, School of Materials Science and Engineering, Hubei University, Wuhan, 430062, P. R. China. E-mail: g.ye0612@hubu.edu.cn*
[d] *Institute of Molecular Aggregation Science, Tianjin University, Tianjin 300072, P. R. China. E-mail: shuyan_shao@tju.edu.cn*

† Electronic supplementary information (ESI) available. See DOI: https://doi.org/10.1039/d5mh00067j

The formula for ZT is expressed as $ZT = S^2\sigma T/\kappa$, where T represents the absolute temperature.[18,19] Due to organic materials' intrinsic low thermal conductivities,[20] the power factor (PF = $S^2\sigma$) is another metric used to evaluate their thermoelectric performance. This is especially useful when measuring κ is complicated or when κ does not change considerably as the other parameters are optimized.

In recent years, we have witnessed significant advancements in organic semiconductor materials for thermoelectrics, driven by a well-developed synthetic toolbox, key building blocks, and optoelectronic materials.[21–28] However, research in this area predominantly focuses on p-type OTE materials. One of the most effective strategies for optimizing p-type materials is the design and implementation of polymeric multi-heterojunctions. This approach significantly enhances interfacial phonon-like scattering, effectively reducing thermal conductivity while ensuring efficient charge transport. As a result, this leads to a remarkable improvement in thermoelectric performance, achieving a ZT value of 1.28 at 368 K.[27] The progress in developing n-type OTE materials lags far behind the p-type counterparts.[29] Another well-known p-type material is PEDOT:PSS, which demonstrates high conductivity exceeding 1000 S cm^{-1} after appropriate treatment.[30,31] Due to the tunable electronic properties of PEDOT:PSS, recent studies have enhanced the thermoelectric performance of flexible PEDOT:PSS fibers by combining them with 1-ethyl-3-methylimidazolium dichloroacetate (EMIM:DCA) and applying subsequent post-treatments with H_2SO_4 and $NaBH_4$, or by employing a triple post-treatment involving H_2SO_4, $NaBH_4$, and EMIM:DCA.[32,33] Additionally, the assembled devices exhibited notable output power density, highlighting the potential for sustainable, self-powered wearable electronic applications. Generally, a complete OTE device requires both p-type and n-type thermoelectric materials with high and comparable performance. However, the development of these materials has been imbalanced, with more focus being directed toward the more challenging n-type OTE materials. Fig. 1(a) shows the trend of maximum power factor (PF_{max}) of n-type materials as a function of publication year. Significant advancements in the PFmax of n-type thermoelectric materials have been observed over the last decade, driven by increasing research efforts. Prior to 2022, only a limited number of materials achieved a PF_{max} of 100 μW m^{-1} K^{-2}, while an increasing number of studies have reported PF_{max} values exceeding 100 μW m^{-1} K^{-2} in recent years, indicating notable progress in the field. The conjugated backbone of these materials plays a crucial role in determining their electronic properties and has led to various molecular design strategies to improve n-type OTE materials, particularly through modifications to the backbone structure. These strategies include halogen substitution to lower the LUMO level,[34] embedding sp^2-N[35] or conformational locking[36] to achieve a planar backbone, exploring acceptor–acceptor (A–A) rather than donor–acceptor (D–A) type backbones,[37] designing fully fused acceptor type polycyclic polymers[38] and developing novel block units.

Extensive research has focused on backbone engineering to design n-type OTE materials that enhance charge mobility and achieve high electrical conductivity.[37,39,40] As shown in Table 1, side-chain engineering is also crucial, as it influences key properties of OTE materials, including solubility, compatibility with dopants, molecular packing, and thin film morphology.[41–44] These factors have a significant impact on the overall performance of OTE materials. To the best of our knowledge, there is a scarcity of well-structured reviews addressing how side-chain engineering impacts the overall performance of n-type OTE materials. This review discusses how the design of side chain molecules affects the properties and performance of n-type organic thermoelectric materials. Firstly, we briefly discuss fundamental concepts and molecular design strategies for n-type OTE materials. We summarize the details of side-chain engineering in n-type OTE materials and demonstrate how a versatile synthetic toolbox can tune various parameters of these materials. Finally, we discuss the current challenges and priorities for future side-chain development.

2. Molecular design considerations for n-type organic thermoelectrics

2.1 Doping principle of n-type molecular doping

Maximizing the Seebeck coefficient and electrical conductivity is essential to achieve high TE performance in organic semiconductors. However, enhancing both the S and σ simultaneously in doped organic semiconductors is challenging.[9]

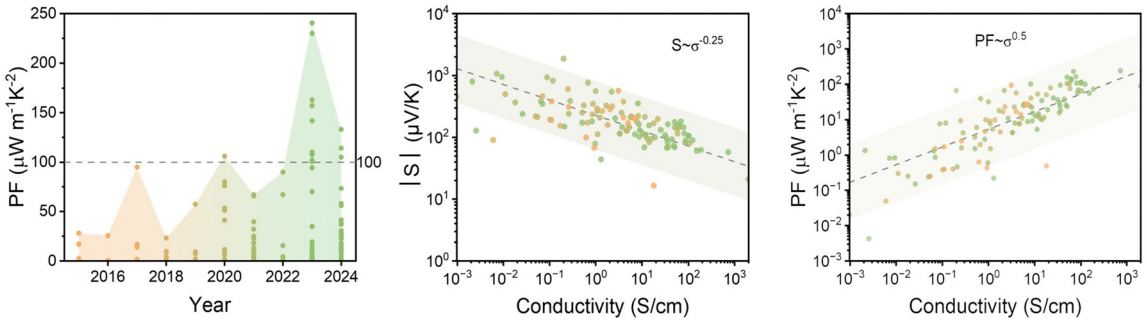

Fig. 1 (a) Power factor of n-type thermoelectrics collected from literature *vs.* year of publication. (b) Absolute Seebeck coefficient and (c) power factor as a function of electrical conductivity showing a universal trend (the majority of the data exhibited a strong correlation with a 95% prediction band derived from the existing dataset). Table S1 (ESI) with the used literature references can be found in the supporting information.

Table 1 Thermoelectric properties of side-chain-engineered materials

Materials	Dopant	σ_{max} (S cm^{-1})	PF_{max} (μW m^{-1} K^{-2})	Ref.
Alkyl side chains				
PNDTI-BBT-DT	N-DMBI	0.18	0.6	45
PNDTI-BBT-DP	N-DMBI	5.0	14.2	45
pNB	N-DMBI	0.011	0.3	46
pNB-Tz	N-DMBI	0.87	9.9	46
pNB-TzDP	N-DMBI	11.6	53.4	46
PNDI2T-1	N-DMBI	0.055	0.45	47
PNDI2T-2	N-DMBI	0.0022	0.00081	47
PNDI2T-1	TAM	0.061	0.33	47
PNDI2T-2	TAM	0.0012	0.0086	47
TBDOPV-2T-118	N-DMBI	0.11	0.76	48
TBDOPV-2T-318	N-DMBI	1.7	~5.7	48
TBDOPV-2T-518	N-DMBI	8.5	23.8	48
PCBM	N-DMBI	0.0116	—	42
N2200	N-DMBI	0.00086	0.01	49
Polar OEG side chains				
PTEG-1	N-DMBI	2.05	16.7	42
PDEG-1	N-DMBI	1.49	9.18	50
PTeEG-1	N-DMBI	2.27	23.1	50
PPEG-1	N-DMBI	1.38	9.76	50
PTEG-2	N-DMBI	8.3	41	23
TEG-N2200	N-DMBI	0.17	0.4	49
PO8	N-DMBI	18.1	14.7	51
PO12	N-DMBI	92.0	94.3	51
PO16	N-DMBI	43.5	62.1	51
P-3O	N-DMBI	9	15.3	52
P-6O	N-DMBI	3.3	4.3	52
P-B3O	N-DMBI	0.03	0.15	52
PNDI2TEG-2Tz	N-DMBI	1.36	3.8	53
Amphipathic side chains				
PNDI2C_8TEG-2Tz	N-DMBI	1.6	16.5	53
PNDI-2O-Tz	N-DMBI	0.63	11.3	54
PNDI-4O-Tz	N-DMBI	2.76	28.4	54
PNDI-8O-Tz	N-DMBI	2.97	26.2	54
OEG side chains and backbone modulation				
PBTI-TEG	N-DMBI	0.2	1.5	55
PDIzTI-TEG	N-DMBI	34	15.7	55
f-BSeI2TEG-T	N-DMBI	11.0	8.8	56
f-BSeI2TEG-FT	N-DMBI	103.5	70.1	56
PDTzTI-T	N-DMBI	73.9	32.4	57
PDTzTI-Se	N-DMBI	98.0	34.6	57
PDTzSI-T	N-DMBI	62.0	16.7	57
PDTzSI-Se	N-DMBI	164	49	57
f-BTI2g-TVT	N-DMBI (Au nanoparticles catalysts)	0.00053	—	34
f-BTI2g-TVTF	N-DMBI (Au nanoparticles catalysts)	19.6	64.2	34
f-BTI2g-TVTCI	N-DMBI (Au nanoparticles catalysts)	7.0	20.2	34
n-PT3	N-DMBI	113.8	110.0	58
n-PT4	N-DMBI	133.3	100.6	58
P-0	N-DMBI	0.012	0.002	59
P-50	N-DMBI	0.76	0.29	59
P-75	N-DMBI	12	13.2	59

As derived by Fritzsche,[16] the S is described as:

$$S = -\frac{k_B}{q}\int \frac{E - E_F}{k_B T}\frac{\sigma(E)}{\sigma}dE \quad (1)$$

where k_B is Boltzmann constant, q is elementary charge, and $\sigma(E)$ is the conductivity distribution function. The charge-transport level is defined as:

$$E_T = \int E\frac{\sigma(E)}{\sigma}dE \quad (2)$$

Then the Seebeck coefficient can be given by:

$$S = -\frac{1}{qT}(E_T - E_F) \quad (3)$$

As implied by eqn (3), the S is determined by the energy difference between the Fermi level (E_F) and the charge-transport level (E_T). Generally, when more charges are generated through molecular doping, the E_F shifts closer to the E_T, decreasing the absolute value of S. On the other hand, both S and σ are intrinsically linked to the charge-carrier density, the S

decreases with charge-carrier density and is given by:[60]

$$S = \frac{8\pi^2 k_B^2}{3qh^2} m^* T \left(\frac{\pi}{3p}\right)^{\frac{2}{3}} \quad (4)$$

where p is charge-carrier density, m^* is effective mass, and h is Planck constant. While the electrical conductivity increases with charge-carrier density, as described by the equation:

$$\sigma = n\mu q \quad (5)$$

where n (in cm^{-3}) is the charge carrier density and μ (in $cm^2\ V^{-1}\ s^{-1}$) is the charge carrier mobility. This trade-off is commonly described by an empirical law of $S \propto \sigma^{-0.25}$, implying that PF increases with σ according to PF $\propto \sigma^{0.5}$.[61] And as such, most efforts have focused on increasing electric conductivity to achieve a large power factor.[22,62,63] Fig. 1(b) and (c) show the evolution of the S and PF as a function of conductivity across a broad range of materials compiled from the literature over the past decade, reconfirming the universal trend. However, some studies reported that certain materials deviated from these empirical laws,[38,42,64,65] with proposed explanations including molecular order, polaron extension, the changes in chemical nature of side chains and doping-induced changes to density of state (DOS). These observations reveal a more complex interdependence than can be explained by empirical models, highlighting the possibility of developing new strategies to simultaneously enhance both electrical conductivity and the Seebeck coefficient. As displayed by eqn (5), the electrical conductivity of doped organic semiconductors is influenced by both charge carrier density and charge carrier mobility (μ). Consequently, to develop high-performance n-type OTE materials, it is essential to achieve high electron mobility and effective n-type doping.[25,66] Therefore, increased focus on molecular doping and the mechanisms of charge carrier transport is necessary.

Taking typical n-type doping as an example, the molecular doping process can be divided into three steps.[67,68] First, n-type organic semiconductors and dopants are mixed through vapor or solution doping. This mixing requires the dopant molecules to disperse and closely interact with the organic semiconductors to facilitate charge transfer. Second, the electrons from the highest occupied molecular orbital (HOMO) or singly occupied molecular orbital (SOMO) of the dopants transfer to the lowest unoccupied molecular orbital (LUMO) of the organic semiconductors (Fig. 2(a)). This transfer generates ionized species *via* integer charge transfer (ICT) or partial charge transfer, which, through molecular orbital hybridization, forms a charge transfer complex (CTC).[69,70] The LUMO of organic semiconductors should be sufficiently deep to ensure that the electron affinity (EA) of the semiconductor is equal to or greater than the ionization energy (IE) of the dopant in the case of ICT. In contrast, the formation of CTC does not require such energy level alignment. The resulting ionized species, radical anions (polaron/bipolaron), are neutralized by surrounding counterions through Coulombic interactions,[71] meaning they cannot directly contribute to the free charge carriers (Fig. 2(b)). Third, free charge carriers are generated when ionized species dissociate from their dopant counterions. This dissociation is strongly influenced by the energetic landscape and electrostatic interactions, leading to a nonlinear variation in conductivity as

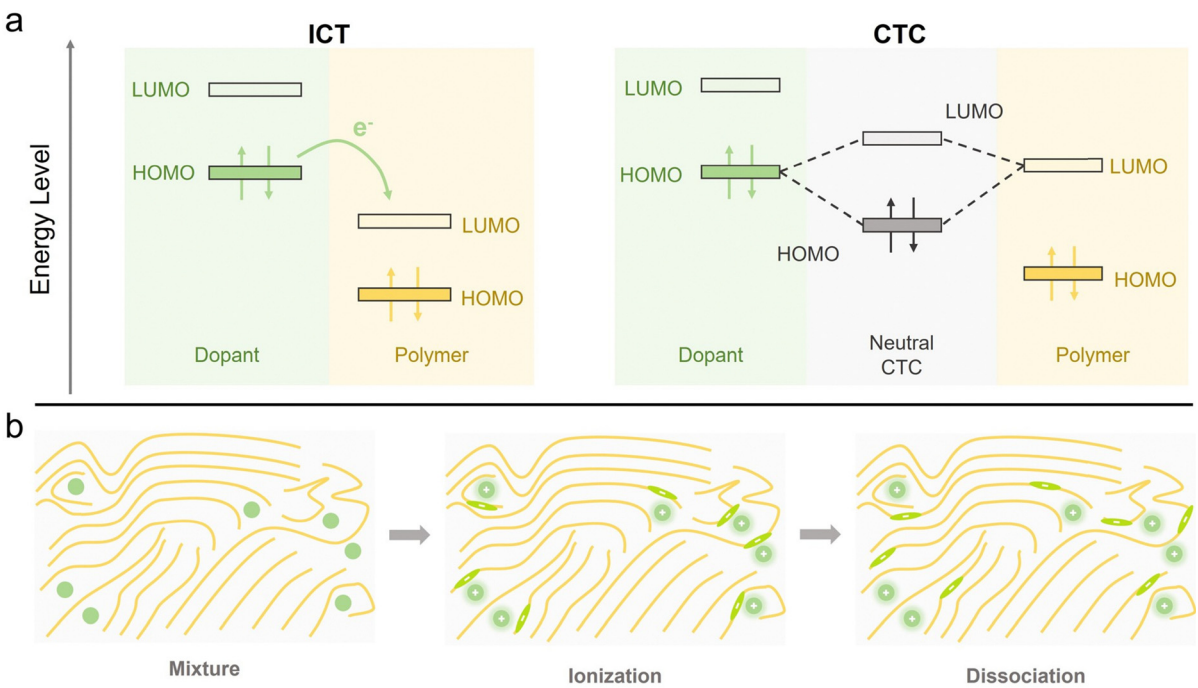

Fig. 2 Schematic representation of the n-doping mechanism and processes: (a) ICT mechanism and partial charge transfer mechanism *via* the formation of CTC, (b) illustration of doping processes (green circles represent dopants and yellow lines represent polymers).

the doping level increases. At low doping levels, dissociation is primarily determined by the Coulomb binding energy between the polaron and dopant, resulting in high dissociation efficiency. Due to trap-filling,[72] conductivity increases superlinearly. At intermediate doping levels, the polaron escapes the Coulomb radius of one counterion but is captured by another, which reduces dissociation efficiency and generates fewer free carriers. Consequently, conductivity increases moderately. At very high doping levels, the Coulomb radius of counterions overlaps, leading to electrostatic screening. In this case, the carrier–dopant interaction weakens, facilitating carrier mobility.[71] However, with more carriers generated, carrier–carrier repulsion becomes non-negligible, which reduces conductivity.[73,74] Additionally, morphological degradation caused by excessive dopants also decreases conductivity at high doping concentrations.[75] Here, we emphasize the weakening effect of a high dielectric constant on Coulomb interactions, which leads to an increase in free carriers. Fig. 3(a) shows the chemical structures of n-type dopants mentioned in this review.

2.2 Strategies to enhance the host/dopant miscibility

Despite significant advancements in organic semiconductors with high electron mobility, achieving high electrical conductivity in n-type doped materials is not guaranteed when the doping efficiency is low. For high doping efficiency, the organic semiconductor must have good miscibility with the dopant. This allows for close contact and facilitates effective charge transfer. Typically, organic semiconductors with high electron mobility exhibit tight π–π stacking and high crystallinity. However, these characteristics can impede the diffusion of dopants, leading to the segregation of dopants from the organic semiconductors.[76,77]

In the past few years, various molecular design strategies have been proposed, focusing on both the side chains and the conjugated backbone of materials to address the issue of miscibility. Side-chain engineering involves polar ethylene glycol-type side chains and changing branching positions within alkyl chains. This topic will be discussed in more detail in the next section. On the other hand, conjugated backbone engineering primarily aims to create space for accommodating dopant molecules, which helps improve miscibility and increase doping efficiency. For example, in BDPPV derivatives reported by Pei (Fig. 3(b)),[78] TBDPPV and TBDOPV-T with amorphous microstructures exhibited improved host-dopant miscibility compared with the TBDOPV-2T, which features rigid planar backbones and ordered microstructures. Perry *et al.* reported a DPP-based D–A conjugated polymer, P(BTP-DPP), with a non-planar donor block.[79] This polymer achieved a high electrical conductivity of 0.45 S cm^{-1} after sequential doping. The non-planar structure of the donor component in the backbone creates space that enhances its miscibility with extrinsic dopant molecules. Sommer *et al.* demonstrated improved host-dopant miscibility using an NDI-2T copolymer incorporating "kinked" monomers.[80] This design creates free space at boundaries, allowing for better accommodation of dopant molecules within the matrix of conjugated polymers.

2.3 Strategies to enhance electron transfer

The energetics of the host and dopant molecules play a crucial role in determining the doping reaction.[81] Over the past decade,

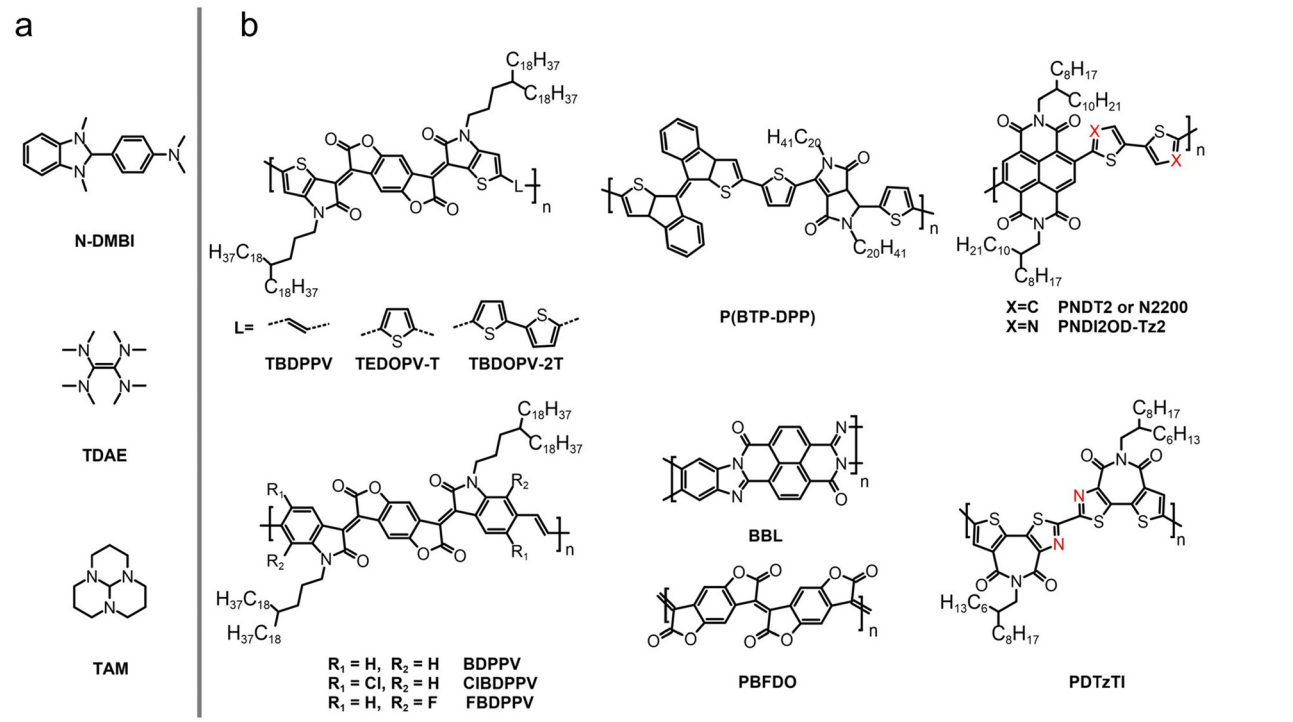

Fig. 3 (a) Chemical structures of n-type dopants mentioned in this review. (b) chemical structures of a selection of polymers mentioned in Section 2.

significant efforts have been focused on developing n-type OTE materials with deep LUMO levels through backbone engineering.[82] For instance, partially thionating the naphthalene diimide (NDI) unit in NDI-based copolymers, such as PNDIT2, leads to a notable decrease in the LUMO energy level, changing from −3.75 eV in PNDIT2 to −3.96 eV in the modified polymer.[83] By replacing bithiophene in PNDIT2 with the more electron-deficient bithiazole, the LUMO energy level of the resulting polymer, PNDI2OD-Tz2, was lowered to −4.10 eV. After n-type doping with TDAE vapor, the electrical conductivity of PNDI2OD-Tz2 was enhanced to 0.1 S cm^{-1}, representing a more than 30-fold increase compared with PNDIT2.[84] This substantial improvement was attributed to its higher doping efficiency and enhanced backbone planarity. Halogen atom substitutions in conjugated polymers have been a facile way to modulate the LUMO energy levels and charge mobilities.[85] For instance, in BDPPV derivatives, compared with pristine BDPPV (−4.01 eV), chloride (Cl)- and fluorine (F)-substituted derivatives, ClBDPPV and FBDPPV exhibited deeper LUMO energy levels of −4.17 eV and −4.30 eV, respectively. Notably, FBDPPV demonstrated the highest electrical conductivity of 14 S cm^{-1} and a power factor of 28 μW m^{-1} K^{-2} after n-type doping. This exceptional TE performance was attributed to its deep LUMO energy level, high doping efficiency, and high electron mobility.

2.4 Strategies to enhance the dissociation of charge-ion pairs

The free charges contributing to the charge transport are generated by dissociating charge-ion pairs formed by the ITC and CTC processes. The efficiency of this dissociation is affected by multiple factors, including the frontier energy levels,[86] the types of counterions,[87] and energetic disorder.[88] Therefore, meticulous molecular designs have been proposed to enhance the charge dissociation of n-doped organic materials. For example, Fabiano and co-workers reported that fully acceptor-fused ladder-type conjugated polymers, such as polybenzimidazobenzophenanthroline (BBL), exhibited higher TE performance after n-type doping, compared with the traditional benchmark n-type D–A conjugated polymer N2200.[38] This was attributed to the linear and torsion-free ladder backbones of BBL, enabling more extensive delocalization of charge carriers. Following this design concept, highly n-doped TE materials with fully fused conjugated backbones, such as poly(*p*-phenylenevinylene) derivatives (LPPV),[36] naphthalene–naphthalene (N–N),[89] and poly(benzodifurandione) (PBFDO),[26] were developed and achieved high TE performance.

Koster and co-workers conducted a comparative study on vapor doping of two n-type conjugated polymers: a twisted D–A type copolymer N2200 and a planar A–A type copolymer PDTzTI.[90] The doped N2200 film exhibited inefficient free charge generation, poor charge transport, and a low power factor of 0.06 μW m^{-1} K^{-2}. In contrast, the doped PDTzTI significantly enhanced free charge generation and transport, resulting in a remarkable conductivity of 4.6 S cm^{-1} and a power factor of 7.6 μW m^{-1} K^{-2}. This study suggests that OTE materials with enhanced molecular planarity, dense molecular packing, and an A–A character promote two-dimensional charge delocalization and facilitate charges escaping from the Coulomb interaction.[91]

2.5 Strategies to improve the charge transport pathway

In n-doped conjugated materials, the delocalization of polarons is a crucial parameter dictating intrachain/interchain charge transport.[37] However, most high-performance n-type conjugated polymers possess D–A structures with substantial torsion angles between the donor and acceptor building blocks. Both theoretical and experimental studies have demonstrated that the HOMO and LUMO orbital coefficients of most twist-backbone D–A polymers are localized on the donor and acceptor fragments, respectively.[37,92] Consequently, this localization of the orbital coefficients leads to the localization of polarons within the backbone, potentially impeding intrachain transport. On the other hand, the interchain transport of carriers is strongly affected by the morphology and microstructure of the film state. Backbone planarity is a crucial factor dictating the conformation of polymer chains in both solution and solid states. Therefore, to optimize n-doping, conjugated polymers should be tailored to exhibit extended polaron delocalization in the charged states, necessitating an exceptionally planar backbone structure. Currently, one effective molecular design strategy is to develop building blocks and modify the backbone to reduce the intermolecular torsion angle through backbone chemistry, such as embedding sp^2-N[35] or conformational locking.[36] This approach achieves a high degree of coplanarity, which in turn improves charge mobility. In addition, side chains can influence film morphology and microstructures,[44] which affect the charge transport of conjugated polymers.

3. Side-chain engineering for n-type organic thermoelectrics

3.1 Alkyl side chains

Generally, alkyl chains are widely incorporated into π-conjugated polymers to modulate their solubility.[93–95] This is essential for solution processing of conjugated polymers, which typically have rigid backbones and compact π–π stacking interactions. Due to the rigid backbone, conjugated polymers exhibit structural stability and unique electronic properties, yet the rigidity also tends to decrease their solubility in common organic solvents. The incorporation of flexible alkyl chains aids in increasing the solubility of conjugated polymers by introducing hydrophobic interactions, which disrupt the tight π–π stacking and increase the spacing between polymer chains.[41,78] It allows for easier processing of conjugated polymers into thin films through solution-based techniques such as spin-coating, dip-coating, or printing.

The side chains also affect backbone conformation[96] and interchain interactions,[97] which are crucial in influencing film morphology and microstructures, ultimately profoundly impacting charge transport. Typically, branched alkyl chains offer advantages in solubilization over linear alkyl chains. Nonetheless, the branched alkyl chain creates a steric hindrance

for the conjugated backbone,[47] potentially affecting the π–π stacking and molecular packing. Therefore, tuning the position of the branching point in branched alkyl chains significantly influences the properties of the polymers,[45,48,98] such as crystallinity, degree of disorder in thin film, and polymer packing orientation, ultimately affecting the device performance.

In 2017, Takimiya *et al.* varied branching positions to synthesize two n-type conjugated polymers, PNDTI-BBT-DP and PNDTI-BBT-DT,[45] which are composed of naphtho[2,3-*b*:6,7-*b*′]dithiophenediimide (NDTI) and benzo[1,2-*c*:4,5-*c*′]-bis[1,2,5]thiadiazole (BBT) units (Fig. 4(a)). PNDTI-BBT-DP features a branched 3-decylpentadecyl side chain, while PNDTI-BBT-DT has a branched 2-decyltetradecyl side chain. The branching point, positioned away from the backbone, improves molecular packing and increases crystallinity in pristine and doped films. This enhancement plays a crucial role in facilitating charge transport, as it helps prevent damage to the crystalline domain caused by the dopant and preserves the orderly morphology of the film. After doping with N-DMBI, the conductivities of PNDTI-BBT-DP and PNDTI-BBT-DT reached values of 5.0 S cm^{-1} and 0.18 S cm^{-1}, respectively. The corresponding power factors for these materials were 14.2 μW m^{-1} K^{-2} and 0.6 μW m^{-1} K^{-2}.

To address the steric hindrance caused by the branched side chain, Zhang *et al.* proposed a new strategy to enhance the

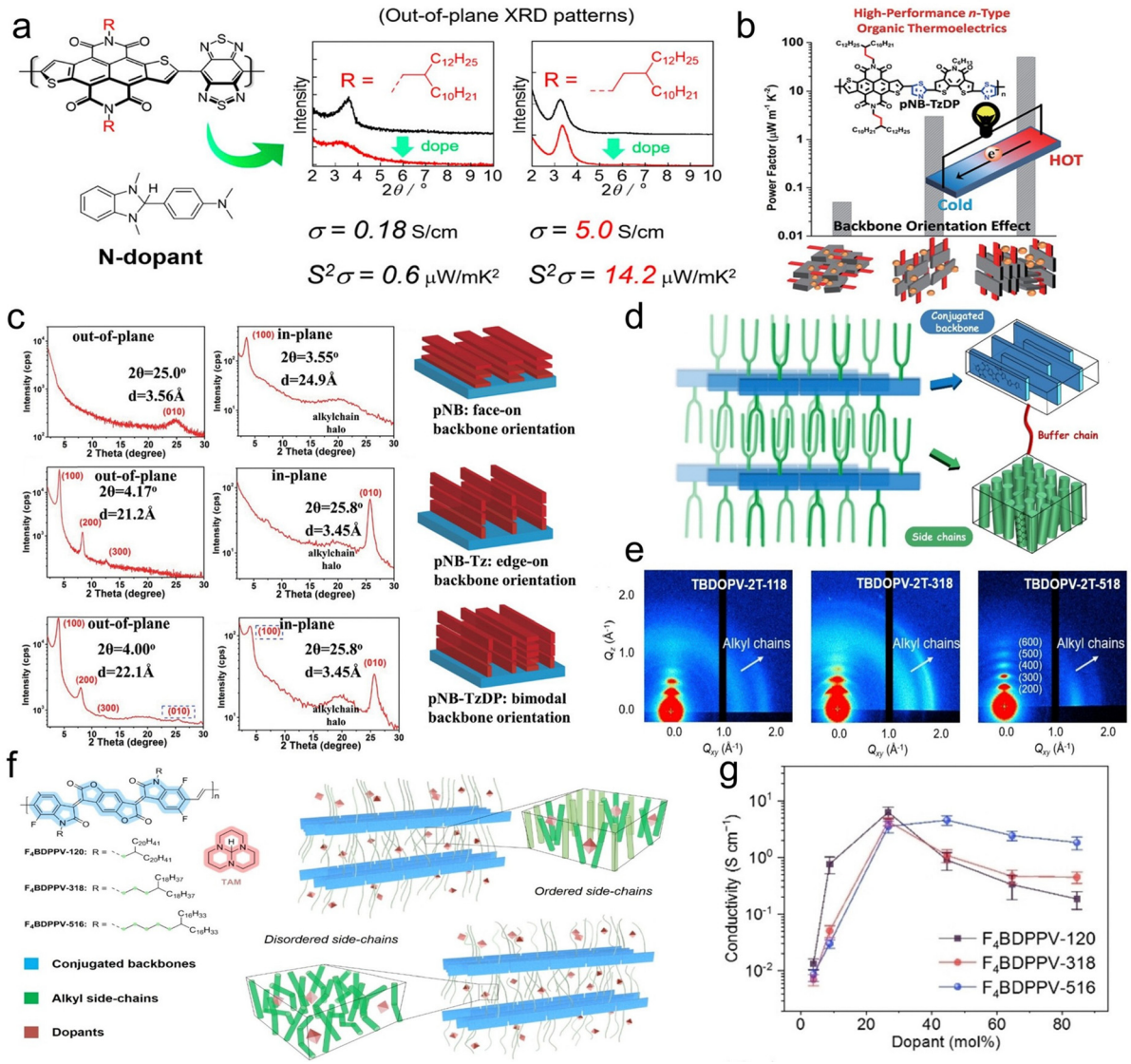

Fig. 4 (a) Molecular designing concept of PNDTI-BBT-DT and PNDTI-BBT-DP. Adapted with permission from ref. 45. Copyright 2017 American Chemical Society. (b) Concept diagram of the side chain design for pNB, pNB-Tz, and pNB-TzDP. (c) GIWAXS patterns of pNB, pNB-Tz, and pNB-TzDP films and corresponding cartoon representations of backbone orientations. Adapted with permission from ref. 46. Copyright 2020 Wang *et al.* under the terms of the Creative Commons CC-BY license. (d) Cartoon representations of buffer chain model. (e) GIWAXS images of TBDOPV-2T-118, TBDOPV-2T-318, and TBDOPV-2T-518 films. Adapted with permission from ref. 48. Copyright 2024 Wiley-VCH GmbH. (f) Schematic representation of the proposed molecular packing models of F4BDPPV polymers. (g) Electrical conductivities of TAM-doped F4BDPPV polymers as a function of dopant fraction. Adapted with permission from ref. 98. Copyright 2022 Wiley-VCH GmbH.

thermoelectric performance of n-doped naphthalene diimide (NDI)–based conjugated polymers.[47] This strategy involves replacing one of the branched side chains with a linear alkyl chain in each NDI unit. The conjugated polymer PNDI2T-1, which has one linear and one branched alkyl chain in each NDI unit, showed superior electrical conductivity and a higher power factor than PNDI2T-2. Both polymers have the same conjugated backbone, but PNDI2T-2 features two branched side chains, and these comparisons were made under the same conditions. The improved thermoelectric performance of the doped PNDI2T-1 films is due to enhanced charge mobility and a higher degree of doping after altering side chains. The packing orientation of conjugated polymers significantly affects charge transport, which can also be modulated by the branching points of the side chains.[99,100] Takimiya and Wang reported three n-type copolymers, pNB, pNB-Tz, and pNB-TzDP,[46] which consist of naphthodithiophenediimide (NDTI) and bithiopheneimide (BTI) units, *via* direct arylation polymerization. Incorporating thiazole units into the polymer backbone and adjusting the branching point of the side chain led to different backbone orientations (see Fig. 4(b)). The polymer pNB, which contains a 2-decyltetradecyl side chain with just one carbon atom between the branch point and the backbone, displayed a face-on orientation with low electron mobility. In contrast, pNB-Tz features 2-decyltetradecyl side chains and includes thiazole units to improve backbone planarity. This resulted in an edge-on orientation with enhanced electron mobility. For pNB-TzDP, the backbone orientation changed significantly, exhibiting a bimodal orientation due to the addition of thiazole units and a 3-decylpentadecyl side chain. X-ray scattering indicated that both the film morphology and the polymer stacking of pNB-TzDP remained unchanged after doping (see Fig. 4(c)). When the dopant ratio reached 50 mol%, the lamellar packing distance of pNB-Tz increased slightly from 21.2 Å to 22.1 Å (see Fig. 4(c)). However, at lower doping concentrations, the morphology of pNB changed considerably, with the lamellar packing distance increasing notably from 24.9 Å to 27.2 Å (see Fig. 4(c)). The dopant had minimal impact on the polymer packing of pNB-TzDP, primarily due to its larger lamellar spacing compared with pNB and pNB-Tz. Among all the materials studied, pNB-TzDP exhibited the highest electrical conductivity of up to 11.6 S cm^{-1} and a power factor of up to 53.4 μW m^{-1} K^{-2}. This outstanding thermoelectric performance can be attributed to the bimodal orientation of pNB-TzDP, which creates three-dimensional conduction channels and facilitates better incorporation of dopants.

Intense crystallization of the side chains may impede the orderly π–π stacking of the conjugated backbones or disrupt the planarity of the conjugated structure. To better understand how branch side chains impact the packing models in semicrystalline conjugated polymers, Pei *et al.* recently proposed a buffer chain model to describe the competition in crystallization between conductive conjugated backbones and insulating side chains (Fig. 4(d)).[48] In this model, the buffer chain links the backbones and branch side chains, which mitigates their mutual restriction and provides a sufficiently free environment for them to crystallize separately and form ordered stacking. Three thiophene-based TBDOPV conjugated polymers, named TBDOPV-2T-118, TBDOPV-2T-318, and TBDOPV-2T-518, have the same semicrystalline conjugated backbone but feature different branch side chains. These polymers feature ethylene, butylene, and hexylene groups as buffer chains, which exhibit distinct molecular packing characteristics. Moving the branching point of the alkyl chain away from the backbone did not significantly decrease the π–π distance. The polymer TBDOPV-2T-518 exhibited higher-order diffraction signals along the Q_z direction up to the distinguishable (600) peak, a more considerable crystalline coherence length (CCL), and a significant reduction in π–π stacking paracrystalline disorder (Fig. 4(e)). As a result, N-DMBI-doped TBDOPV-2T-518 achieved the highest n-type conductivity of up to 8.5 S cm^{-1}, along with the highest power factor of 23.8 μW m^{-1} K^{-2}.

Pei *et al.* reported a strategy to achieve efficient charge-transport and improve doping miscibility in n-doped conjugated polymers by moving the branching point far away from the conjugated backbone.[98] Three conjugated polymers, F_4BDPPV-120, F_4BDPPV-318, and F_4BDPPV-516, based on a tetrafluorinated benzodifurandione-based poly(*p*-phenylene vinylene) (F_4BDPPV) backbone, with different branched alkyl chains resulting from moving the branching point away from the conjugated backbone: 2-icosyldocosyl, 4-octadecyldocosyl, and 6-hexadecyldocosyl (Fig. 4(f)). Upon molecular doping, the side chain with a more distant branching point provides additional space for accommodating extrinsic dopants, without disrupting the original packing of the conjugated backbone or the charge transport channels. Consequently, improved morphology and stable, higher conductivity under overloading dopant are achieved in F_4BDPPV-516, which exhibited the maximal conductivity of 5.3 S cm^{-1} at 45 mol% TAM doped, when the other two polymers showed declined conductivities (Fig. 4(g)). This work demonstrated that the molecular interactions between polymer side-chain and dopants can be controlled by the branch point of the side-chain, realizing effective n-doping without sacrificing the interchain π–π stacking. Fig. 5 lists the chemical structures of the mentioned polymers featuring alkyl side chains.

3.2 Oligo (ethylene glycol) (OEG)-based side-chain engineering

3.2.1 Polar linear OEG side chains. As discussed in the last sections, alkyl side chains have been used to regulate the miscibility in doped conjugated polymers. Another innovative approach to address this issue is to adjust the polarity of the conjugated polymers and dopants to a compatible level by incorporating polar oligo (ethylene glycol)-type side chains. In 2017, Koster and Liu *et al.* reported a strategy to achieve efficient charge-transport and high doping miscibility in fullerene derivate with OEG side chains (PTEG-1).[42] After doping with N-DMBI, the conductivity achieved a maximum of 2.05 S cm^{-1} and a power factor of 16.7 μW m^{-1} K^{-2} at 40 mol% doping concentration (Fig. 6(b)). The doping efficiency of PTEG-1 significantly improved to approximately 18%, compared with less than 1% for a nonpolar reference fullerene derivative, PCBM (Fig. 6(e)).

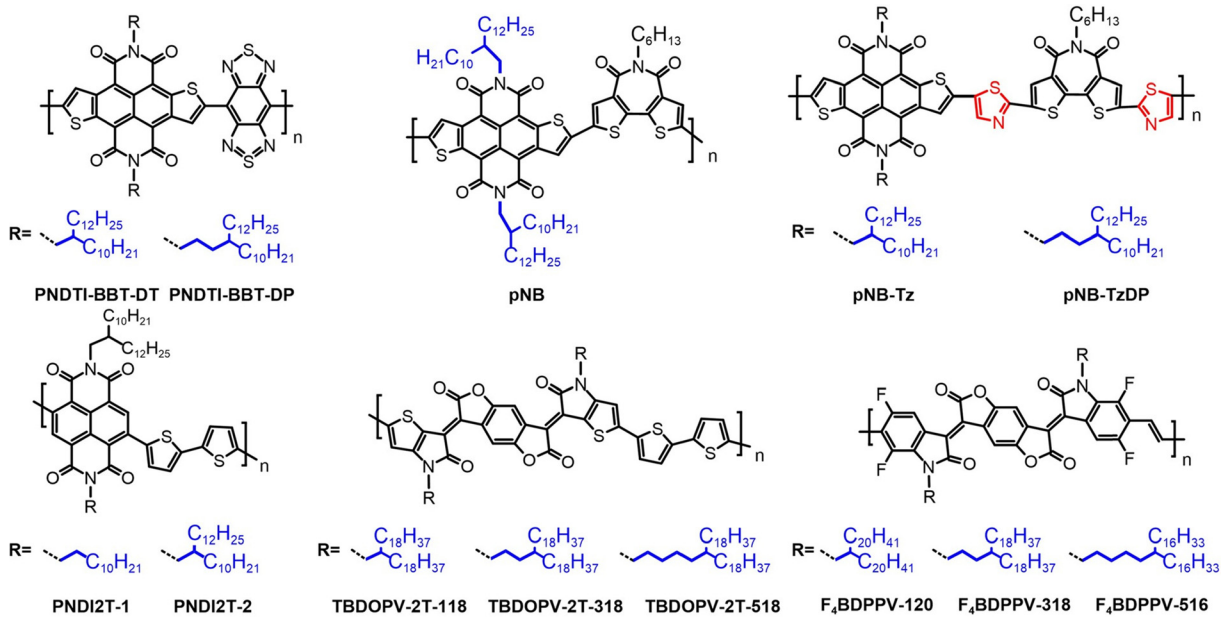

Fig. 5 Chemical structure of the mentioned polymer with alkyl side chains.

During molecular doping, when the ionization step of the doping reaction occurs, the dopant becomes more polar than apolar host molecules. The polarity difference leads to phase separation, especially at high doping levels. In the case of PTEG-1, incorporating polar TEG side chains enhanced the polarity of the host. It allowed for better dopant miscibility, facilitating charge transfer and higher doping efficiency than PCBM. Furthermore, the dopants were preferentially incorporated into the TEG side chain domains, and the π–π stacking of PTEG-1 was not disrupted and preserved, leading to enhanced thermal stability. Inspired by this strategy, Qiu *et al.*[101] synthesized a novel DMBI derivative functionalized with a triethylene glycol side chain (TEG-DMBI) to further enhance dopant-host miscibility in the PTEG-1 system. Compared with N-DMBI-doped PTEG-1, the TEG-DMBI doped system demonstrated superior doping efficiency at intermediate concentrations, achieving a higher PF of 19.1 μW m^{-1} K^{-2}. They attributed the enhanced doping efficiency to better miscibility in the as-prepared state. Moreover, different dopants exhibited varying miscibility with polymers containing OEG side chains, leading to differences in doping efficiency.[102] Therefore, selecting a dopant that is compatible with the specific polymer is crucial for achieving efficient doping. Later, this molecular design strategy was further successfully extended to the benchmark n-type polymer, N2200, with its naphthalenediimide-bithiophene (NDI-2T) conjugated backbone, by the same research group,[49] as well as by the Müller group[103] and Sommer group,[104] respectively. Specifically, Koster and Liu *et al.*[49] developed the n-type conjugated polymer TEG-N2200, which carried polar triethylene glycol side chains on the NDI unit, exhibited an optimized spatial distribution of dopants, and achieved an enhanced electron conductivity of 0.17 S cm^{-1}. This conductivity is 200 times greater than that of N2200 with traditional alkyl side chains (Fig. 6(d)), due to the improved dispersion of N-DMBI molecules within the TEG-N2200 matrix and a one-order magnitude enhancement in doping efficiency. Coarse-grained molecular dynamics simulations suggested that the required free energy for transferring an N-DMBI molecule from the alkyl phase to the TEG phase is −16 kJ mol^{-1} therefore, the n-type dopant molecules would rather move to the TEG phase than the alkyl chain phase (Fig. 6(f) and (g)). Likewise, the Müller group reported a n-type conjugated polymer, p(gNDI-gT2), based on an NDI-T2 backbone with oligoethylene glycol (OEG) side chains on NDI and 2T units.[103] After doping with N-DMBI, p(gNDI-gT2) achieved an enhanced molecular doping efficiency of up to 13%, leading to a high conductivity of above 0.1 S cm^{-1} and a power factor of 0.4 μW m^{-1} K^{-2}, attributed to the enhanced miscibility of dopants in a polymer matrix. These studies highlight the importance of OEG side chains in enhancing miscibility, thereby improving doping efficiency.

To gain a deeper understanding of the critical role of the OEG-type side chain in molecular doping, Koster and Liu conducted a comparison study between PTEG-1 (dielectric constants $\varepsilon_r \approx 5.9$) and PCBM ($\varepsilon_r \approx 3.7$) in a slightly doped system.[105] In this system, a very small amount of dopant molecules is typically well-dispersed in the host matrix due to entropy, making it a good platform for exploring the doping mechanism at a quasi-molecular level. The doping efficiency of lightly doped PCBM layers was limited to a few percent, but doped PTEG-1 films exhibit very high doping efficiency approaching 100%. The enhanced molecular doping of PTEG-1 is attributed to the electrostatic interaction between the charge transfer complex and the polar environment created by the C–O bonds in the side chains of PTEG-1. This polar environment screens the electric fields created by counterions, facilitating the creation of free carriers (Fig. 6(a)). In other words, the high local permittivity

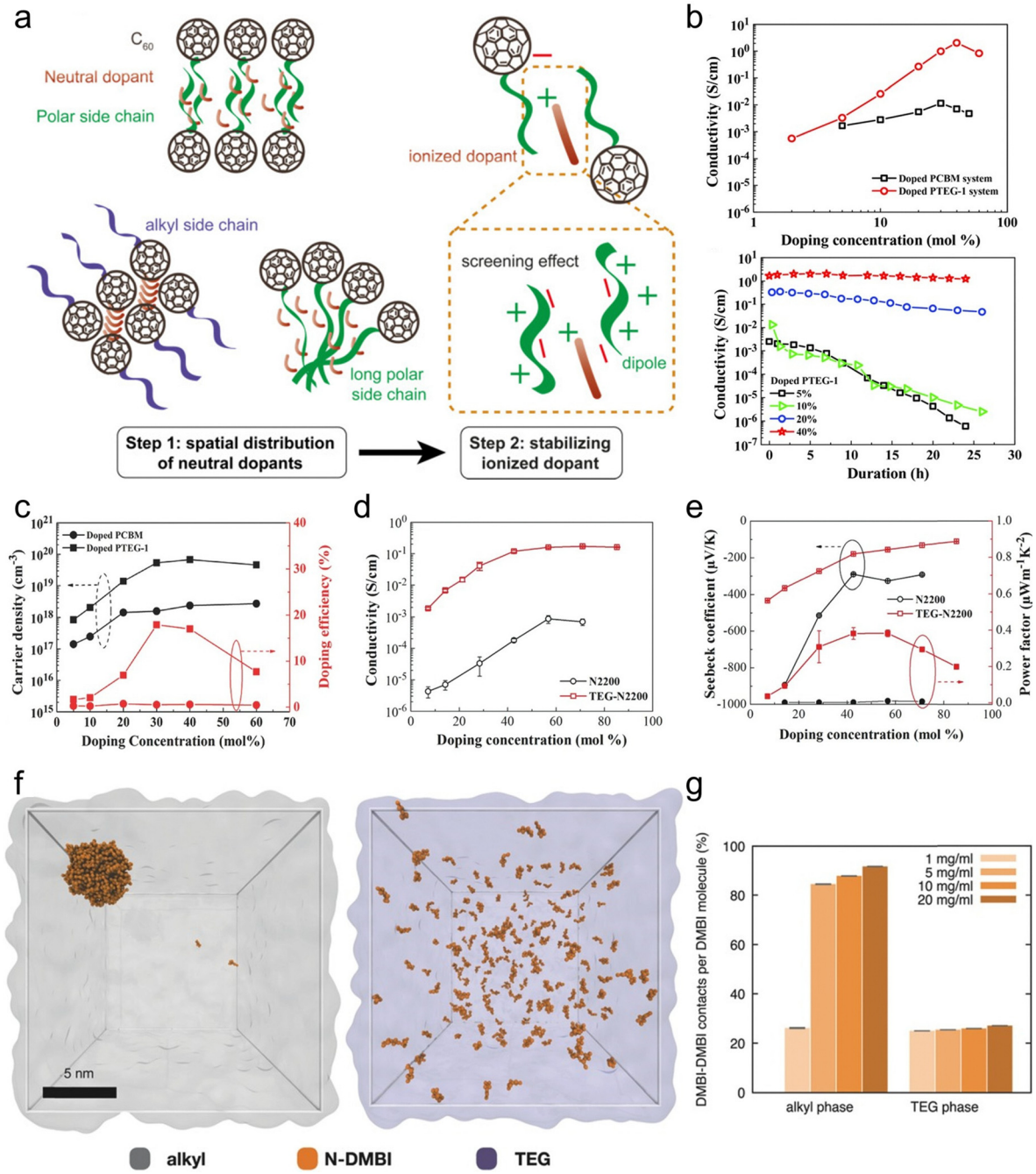

Fig. 6 (a) Illustration of OEG side chain functions: enhancing dopant/host miscibility and creating electrostatic screening. Adapted with permission from ref. 50. Copyright 2018 Elsevier Ltd. (b) Conductivity and stability under various doping concentrations of doped PTEG-1. (c) Carrier density and doping efficiency under various doping concentrations of doped PCBM and PTEG-1. Adapted with permission from ref. 42. Copyright 2017 Liu *et al.* under the terms of Creative Commons CC-BY-NC-ND license. (d) Conductivity and (e) Seebeck coefficient under various doping concentrations of doped N2200 and TEG-N2200. (f) Dynamics simulations of n-DMBI molecules within a pure N2200 side chain matrix and a pure TEG-N2200 side chain matrix. (g) The normalized contact count between dopant molecules in the two matrices. Adapted with permission from ref. 49. Copyright 2018 Wiley-VCH Verlag GmbH & Co.

of PTEG-1 with OEG side chains reduced the Coulomb binding energy from surrounding counter ions, which facilitated the dissociation of CTC and resulted in a lower activation energy for carrier generation compared with PCBM.

3.2.2 Effects of OEG Chain length and branching on n-type organic thermoelectrics. Both the type of side chains and their geometry significantly impact molecular packing and thermoelectric performance. Liu *et al.* investigated a series of fullerene derivatives (PDEG-1, PTEG-1, PTeEG-1, PPEG-1) that have varying OEG side chain lengths, ranging from diethylene glycol to pentaethylene glycol, to explore their impacts on n-type organic thermoelectric behavior.[50] Due to the polar OEG side chains,

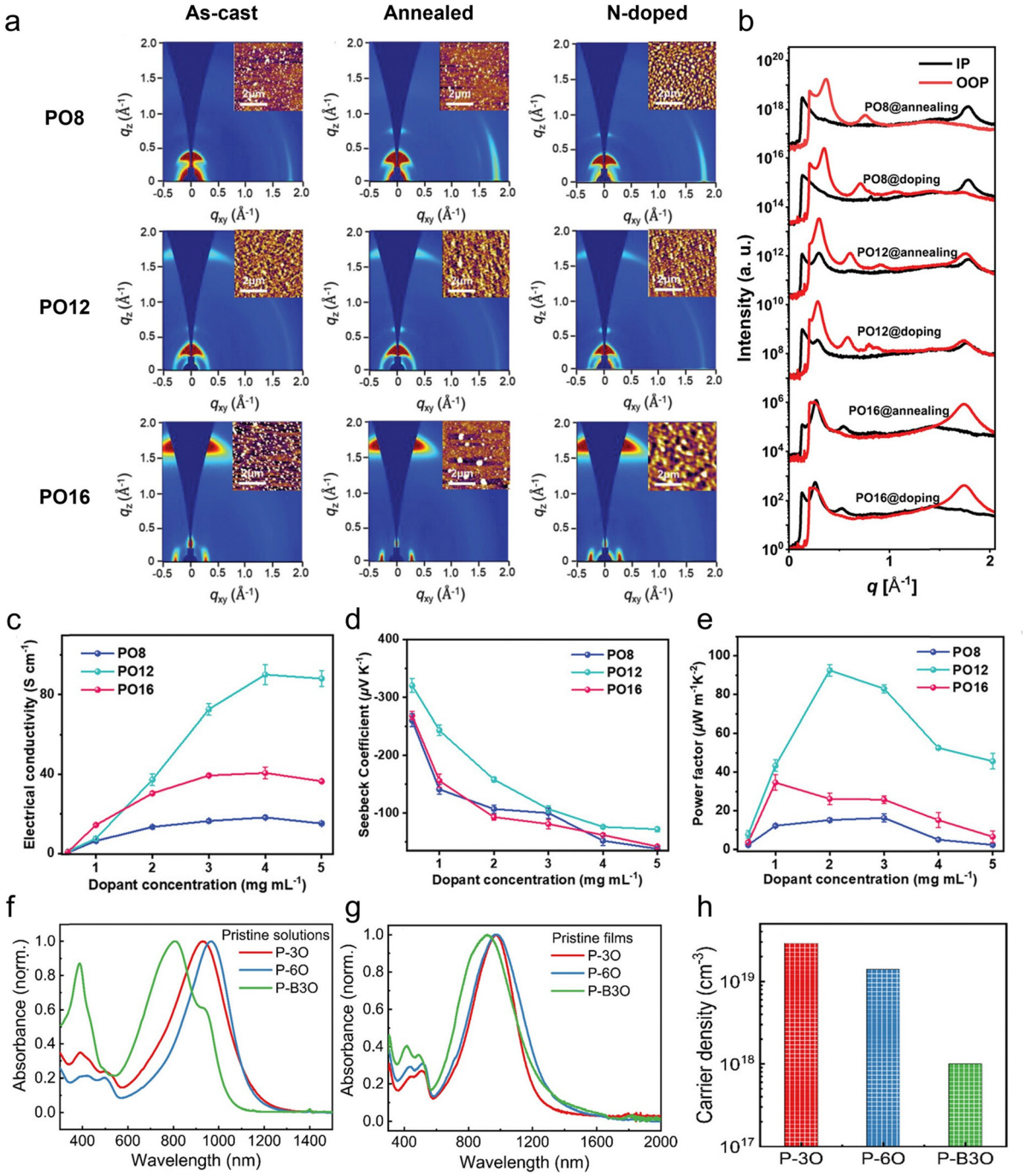

Fig. 7 (a) GIWAXS images and AFM height images (inset) of PO8, PO12 and PO16. (b) The corresponding line-cut profiles of the GIWAXS images of PO8, PO12, and PO16. (c) Conductivity, (d) Seebeck coefficient, and (e) power factor of doped PO8, PO12, and PO16. Adapted with permission from ref. 51. Copyright 2023 Feng *et al.* under the terms of the Creative Commons CC-BY license. UV-Vis-NIR absorption spectra of (f) pristine solutions and (g) pristine films of P-3O, P-6O, and P-B3O, (h) carrier density of doped P-3O, P-6O, and P-B3O at a concentration of 5 wt%. Adapted with permission from ref. 52. Copyright 2024 Yang *et al.* under the terms of the Creative Commons CC-BY license.

all fullerene derivatives have good miscibility with the dopant, exhibiting less phase aggregation and increasing the doping efficiency. In addition, the molecular packing can also be improved by controlling the length of OEG side chains. The PTeEG-1, with an optimal OEG side chain length, demonstrated the highest crystallinity and most extensive superlattice domains, indicating superior molecular order, resulting in a high electrical conductivity of 2.27 S cm^{-1} and a power factor of 23.1 μW m^{-1} K^{-2}. This study also noted that fullerene derivatives with excessively long OEG side chains exhibited reduced thermoelectric performance due to the dilution of conjugated moieties.

Within the framework of the phonon-glass electron-crystal, (PGEC) concept,[106,107] numerous efforts have been made to develop ideal thermoelectric materials, but no material has yet fully realized this concept. Moreover, the PGEC concept was originally proposed for inorganic materials. In 2020, Koster and Liu introduced the definition of organic PGEC: (i) the thermal conductivity should reach the amorphous limit of the material, and (ii) the charge carrier mobility should reach its crystalline limit.[23] Specifically, they reported a fullerene derivative, PTEG-2, with ''arm-shaped'' double-triethylene-glycol-type side chains that approach an organic PGEC material. This unique side chain geometry induces a morphology transition from disorder to order and promotes the formation of a thermodynamically stable state after thermal annealing, resulting in excellent thermal stability. When doped with N-DMBI, PTEG-2 exhibited a high conductivity of 8.3 S cm^{-1}. The bulk mobility of the doped PTEG-2 was measured at 1.2 cm^2 V^{-1} s^{-1}. Compared with single-crystal C60, this value suggests that PTEG-2 aligns with the electron-crystal concept. Furthermore, the thermal conductivity of PTEG-2 was recorded at 0.086 W m^{-1} K^{-1} at room temperature and increased slightly to 0.097 W m^{-1} K^{-1} at 120 °C. This indicates that PTEG-2 closely approaches the phonon-glass concept. Consequently, PTEG-2 achieved an impressive *ZT* value of 0.34 at 120 °C.

In addition to fullerene derivatives, the geometry of side chains can also adjust the molecular packing and doping of conjugated polymers. Guo *et al.* investigated a series of fused bithiophene imide dimer-based n-type conjugated polymers (PO8, PO12, and PO16) carrying branched OEG side chains of varying lengths.[51] As the side-chain size increases, the molecular packing changes from an edge-on orientation of P-O8 to a bimodal orientation of PO12 and finally to a face-on orientation of P-O16 (Fig. 7(a) and (b)). Meanwhile, the crystalline domains of the polymer gradually decrease in size. Consequently, these three polymers exhibit a monotonic decrease in electron mobility as the side-chain size increases, due to the gradual lowering of film crystallinity and the change in backbone orientation. However, after n-type molecular doping, conjugated polymer PO12, with a moderate side chain length, exhibited the optimum OTE performance (Fig. 7(c)–(e)), attributed to the high doping efficiency, large charge mobility, and 3D conduction channel derived from bimodal orientation.

Very recently, Koster and Chiechi reported on three n-type conjugated polymers (P-3O, P-6O, and P-B3O) that comprise a naphthalenediimide–dialkoxybithiazole backbone but have different linear lengths or branched OEG side chains.[52] When doped with N-DMBI, all these polymers exhibited good host/dopant miscibility. In the linear OEG side-chain-based polymers (P-3O and P-6O), the increased volume of OEG side chains slightly influences the planarity of backbones, thereby leading to similar and satisfactory thermoelectric performances. P-B3O, with the same OEG volume as P-6O but adopting a branched type, displayed a twisted backbone due to the steric hindrance introduced by the branched OEG side chain. As a result, the conjugated backbones exhibit reduced planarity and rigidity, leading to critical molecular packing changes, low charge carrier mobility and doping efficiency, and, thus, low thermoelectric performance. The reduced planarity of the P-B3O backbone was verified by density functional theory (DFT) calculations and the red-shift of absorption maxima peak relative to P-3O and P-6O in the UV-Vis-NIR absorption spectrum (Fig. 7(f) and (g)). Moreover, the P-B3O exhibited the strongest quenching of neutral peak in the absorption spectrum but the lowest densities of carrier measured by MIS devices (Fig. 7(h)) after being doped with N-DMBI at the concentration of 5 wt%. This indicated that P-B3O could easily accept the electron from dopants to form CTC states, likely due to the increased number of reactive sites provided by branched OEG side chains. However, the dissociation of CTC is suppressed. There is no well-established general rule or experimental validation regarding the impact of the length and branching of polar OEG side chains, necessitating further research for informed molecular structure design. Fig. 8 lists the chemical structures of the mentioned polymer with polar OEG side chains.

As such, the geometry of OEG side chains, including their length and branching points, plays a crucial role in determining intermolecular interactions. This, in turn, significantly impacts molecular ordering, film microstructure, and morphology, ultimately affecting the performance of organic thermoelectric (OTE) materials. A thorough investigation of OEG side chains highlights the importance of carefully fine-tuning their lengths and branching points to enhance thermoelectric performance effectively.

3.3 Amphipathic side chains for OTE

Recently, there has been a growing interest in exploring the negative effect of Coulomb interactions between polarons/bipolarons and counterions on molecular doping and Seebeck coefficient and electrical conductivity in doped OTE materials.[90,108] In a theoretical study, Koster *et al.* highlighted the role of Coulomb interactions on the Seebeck coefficient. They discovered that carrier–carrier interactions can decrease the Seebeck coefficient at high dopant loading.[109] To overcome the limitations caused by Coulomb interactions, Liu *et al.* explored amphipathic side chains as a new molecular strategy to selectively enhance the Seebeck coefficient without sacrificing electrical conductivity.[53] An NDI-based n-type conjugated polymer, PNDI2C8-TEG-2Tz, was reported, whose amphipathic side chains consist of an alkyl chain segment as a spacer between the conjugated backbone and an ethylene glycol-type chain segment (Fig. 9(a)). Incorporating alkyl chain spacers in the conjugated polymer film helps reduce energetic disorder and effectively positions dopant molecules away from the polymer backbone. This arrangement minimizes the adverse effects of Coulomb interactions from the counterions. Kinetic Monte Carlo simulations have shown that increasing the distance between the host polymer and the dopant lowers Coulombic interactions, enhancing the Seebeck coefficient for a given electrical conductivity. As a result, the doped polymer film with amphipathic side chains achieved an optimized electrical conductivity of 1.6 S cm^{-1} and a power factor of 18 μW m^{-1} K^{-2} (see Fig. 9(b) and (c)). This performance represents an approximately

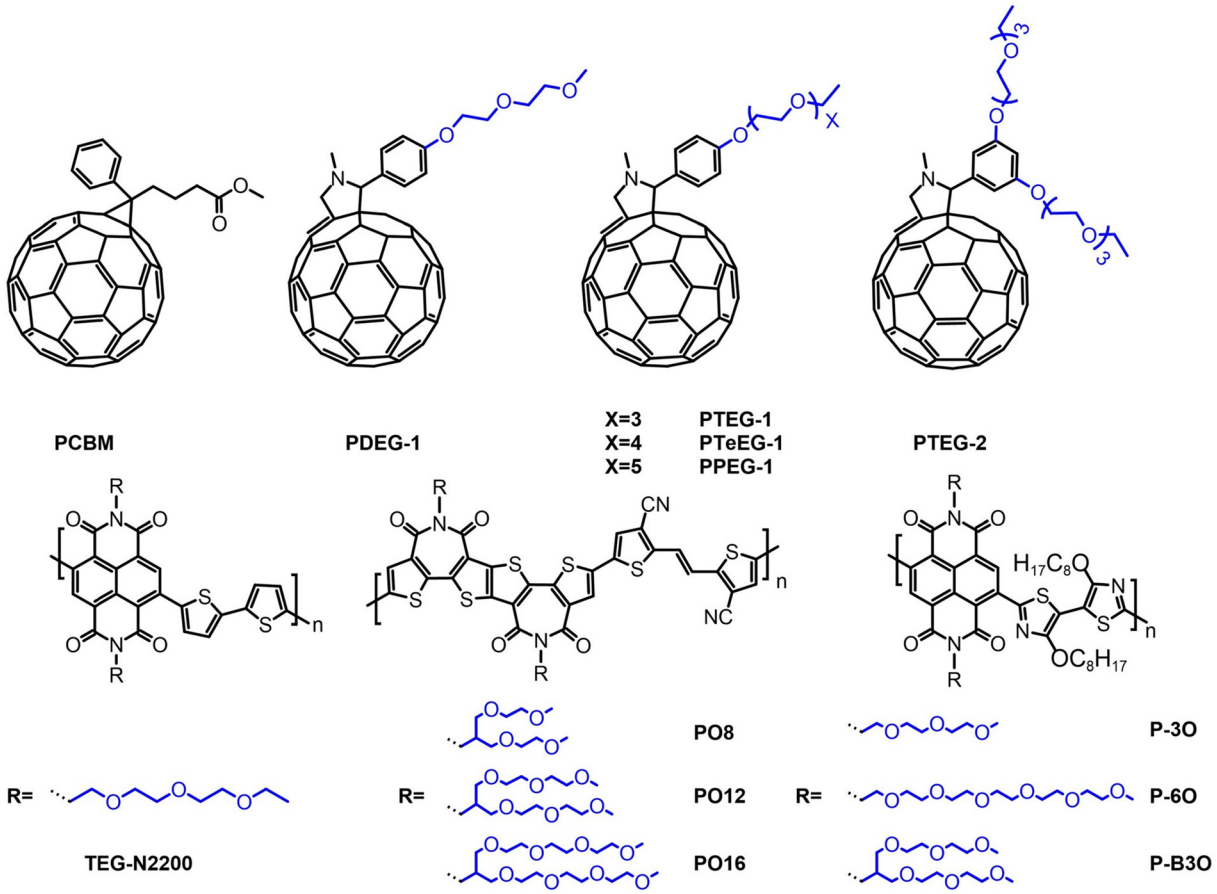

Fig. 8 Chemical structure of mentioned polymer with polar OEG side chains.

fivefold improvement compared with the reference polymer, PNDI2TEG-2Tz, which features polar OEG side chains.

Recently, Liu *et al.* tailored amphipathic side chains by controlling the length of the end groups.[54] They reported three n-type conjugated polymers (PNDI-2O-Tz, PNDI-4O-Tz, and PNDI-8O-Tz) that consist of a naphthalenediimide–dialkoxybithiazole backbone and feature amphipathic side chains with varying OEG lengths. All these polymers exhibited relatively high Seebeck coefficient (340–490 μV K^{-1}) at an optimal doping concentration compared with reported n-type OTE polymers (with a Seebeck coefficient of 100–200 μV K^{-1}),[22,96,102,110–112] due to their amphipathic side chains minimizing the negative influence of Coulomb interactions from the counterions. The polymer with longer amphipathic side chains improves miscibility between the host and the dopant. Therefore, as the length of the oligoethylene glycol end group increases, the maximum electrical conductivity is achieved at a lower doping concentration. However, excessively glycol end group can disrupt the lamellar packing. In addition, the insulating OEG side chains reduced the concentration of conjugated segments, thereby hindering charge transport. As a result, the PNDI-4O-Tz with a medium-length glycol side chain exhibited optimized host/dopant miscibility and compact packing, leading to a high conductivity of 2.76 S cm^{-1} and a power factor of 28.4 μW m^{-1} K^{-2}.

3.4 Glycol side chains prevail in molecular design

Since polar ethylene glycol-type side chains are very effective for facilitating doping and boosting charge transport, they have been widely used in designing new n-type OTE polymers. Fig. 10 lists the chemical structures of those newly designed n-type conjugated polymers featuring ethylene glycol-type side chains. Koster and Liu *et al.* tailored the DOS through backbone chemistry.[35] They replaced two thiophene units with weaker donor thiazole units in the PNDI2TEG-2T backbone and synthesized PNDI2TEG-2Tz. Ethylene glycol-type side chains functionalized both polymers for sufficient host/dopant miscibility. The introduction of sp^2-nitrogen atoms led to a downshift in the LUMO level, enhanced the planarity of the backbone (see Fig. 11(a)), and narrowed the DOS distribution compared with PNDI2TEG-2T. These changes ultimately enhanced both the conductivity and the Seebeck coefficient. Additionally, the improved miscibility of dopants due to the OEG side chains allowed PNDI2TEG-2Tz to achieve a high conductivity of 1.8 S cm^{-1} and a power factor of 4.5 μW m^{-1} K^{-2} (Fig. 11(b) and (c)).

To systematically explore the influence of the backbone on OTE performance, Gou *et al.*[55] synthesized a series of thiazole imide-based polymers, each containing a distinct backbone type: PDTzTI-TEG-T (A–D), PDTzTI-TEG-FT (A–WD), PBTI-TEG

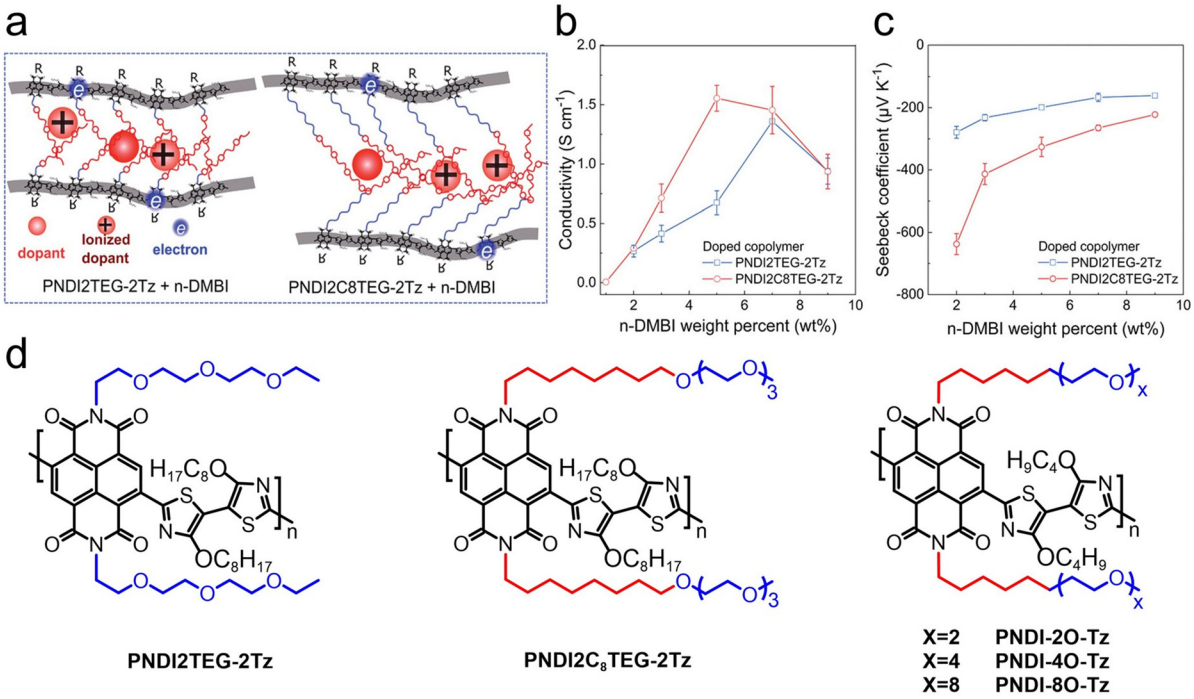

Fig. 9 (a) An illustration of controlling the distance between the dopant and the backbone through amphiphilic side chain design. Conductivity (b) and (c) Seebeck coefficient under various doping concentrations of PNDI2C8TEG-2Tz and PNDI2TEG-2Tz. Adapted with permission from ref. 53. Copyright 2020 Liu *et al.* under the terms of Creative Commons CC-BY-NC-ND license. (d) Chemical structure of the mentioned polymer with amphipathic side chains.

(A–A), and PDTzTI-TEG (A–A), with all polymers incorporating branched OEG side chains. Compared with PBTI-TEG, introducing thiazole units lowered the LUMO level, leading to more efficient molecular doping and higher conductivity. With the weakening of the donor character from PDTzTI-TEG-T to PDTzTI-TEG-FT and to PDTzTI-TEG, the LUMO levels lowered, and field-effect charge mobility increased. Besides, incorporating OEG side chains enhances the dopant's miscibility. Further, it reduces the LUMO level compared with PDTzTI and PBTI with alkyl side chains, facilitating the doping reaction and, thus, enhancing OTE performance. After being doped with N-DMBI, PDTzTI-TEG achieved a maximum conductivity of 34 S cm^{-1} and a PF of 15.7 μW m^{-1} K^{-2}.

The BTI-based polymers have exhibited the potential of OTE materials but are limited by their high-lying LUMO level. Guo and co-workers used the selenium-substitution strategy to optimize the OTE performance and synthesize f-BSeI2TEG-FT and nonfluorinated counterpart f-BSeI2TEG-T.[56] The selenium substitution can significantly lower the LUMO levels of the two polymers by about 0.2 eV and improve the electron mobility by two orders of magnitude compared with sulfur analogs. Due to the additional electron-withdrawing fluorine atoms, which weakened the donor character of the thiophene moiety, f-BSeI2TEG-FT exhibited a further lowered LUMO level, resulting in enhanced molecular doping. With the synergistic effects of optimized backbone and OEG side chains, f-BSeI2TEG-FT finally achieved an impressive electrical conductivity of 103.5 S cm^{-1} and a power factor of 70.1 μW m^{-1} K^{-2} after sequentially doping with N-DMBI using the Au nanoparticles catalyzed doping technique. Aiming to gain deeper insights into the effects of selenium atom incorporation, Guo and co-workers developed a series of A–WD type polymers based on thiazole imide unit, differing in content and position of selenophene substitution, named PDTzTI-T, PDTzTI-Se, PDTzSI-T, and PDTzSI-Se (Fig. 11(d)).[57] As the selenophene content increased, the polymers exhibited a lower LUMO level and a more planar backbone (Fig. 11(e) and (f)). Moreover, introducing selenium atoms reduced crystallinity in the neat films, which may facilitate better penetration of dopant molecules. All selenophene-containing polymers showed improved crystallinity after doping with N-DMBI compared with the neat films. Among these polymers, PDTzSI-Se demonstrated the best thermoelectric performance, with a maximum conductivity of 166.3 S cm^{-1} and a power factor of 54.2 μW m^{-1} K^{-2}.

Very recently, Guo *et al.* reported on two polymers that incorporate a fused bithiophene imide dimer (f-BTI2) as the acceptor unit, along with halogenated thienylene–vinylene–thienylene (TVT) as the weak donor co-unit featuring branched oligo(ethylene glycol) (OEG) side chains.[34] These polymers, named f-BTI2g-TVTF and f-BTI2g-TVTCl, were employed as organic mixed ionic–electronic conductors in both organic electrochemical transistors (OECT) and organic thermoelectric devices (OTE). Introducing halogen groups with strong electron-withdrawing ability into the backbone lowered the LUMO level and increased the polarity, facilitating the doping reaction. The fluorinated f-BTI2g-TVTF exhibited remarkable

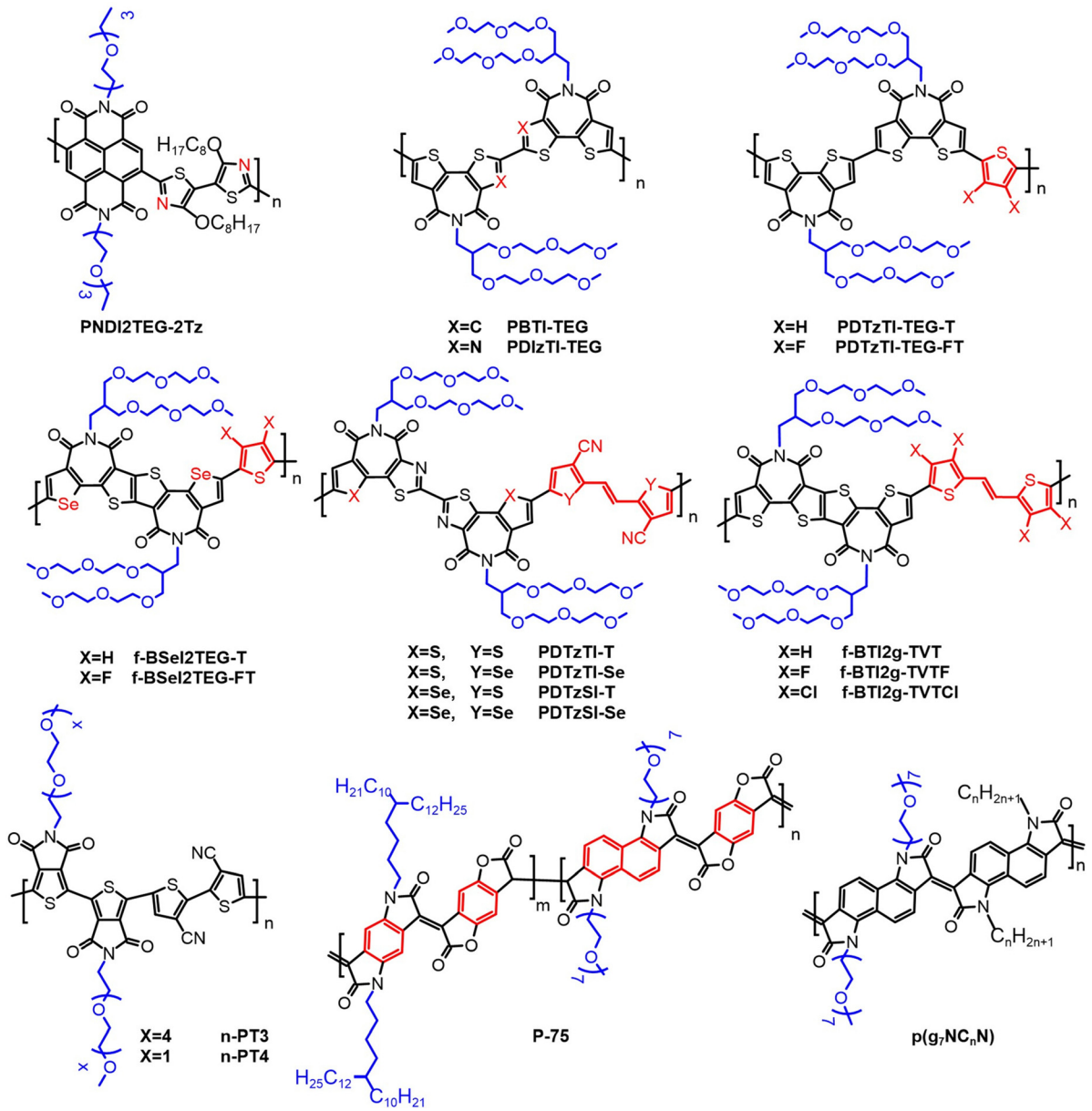

Fig. 10 Chemical structures of backbone optimized polymers with OEG side chains, as discussed in Section 3.

performance in OTE with a conductivity of 19.6 S cm^{-1} and a power factor of 64.2 μW m^{-1} K^{-2}.

The conductivity dramatically drops at over-high doping loading in most cases due to the morphological degradation. In contrast, Deng *et al.* developed two A–WD type polythiophene derivatives named n-PT3 and n-PT4 with different OEG side chain lengths, exhibiting high doping loading tolerance.[58] OEG side chains improve the solubility in alcohol and host/dopant miscibility. Thus, both conjugated polymers exhibited high electrical conductivity exceeding 100 S cm^{-1} after being doped with N-DMBI. Notably, they maintained this high conductivity even at an exceptionally high doping concentration of 250 mol% (Fig. 11(h) and (i)). This remarkable performance was attributed to their robust ability to mitigate backbone twisting and prevent morphological degradation at saturated doping levels. Furthermore, the doping-induced molecular order improved the crystal structure and allowed for the retention of crystallinity (Fig. 11(g)).

Leveraging the benefits of A–A type polymers and rigid backbone, McCulloch and co-workers reported three lactone-based fully fused polymers (named P-0, P-50, and P-75) with all acceptor properties varying in density of lactone group, which were enabled by adjusting the content of benzene.[59] As the benzene content increases, the polymers demonstrate a greater electronic affinity (EA) due to a higher density of electron-withdrawing groups, making the n-doping reaction thermodynamically favourable. Additionally, the increased benzene content promotes planarization of the polymer backbone,

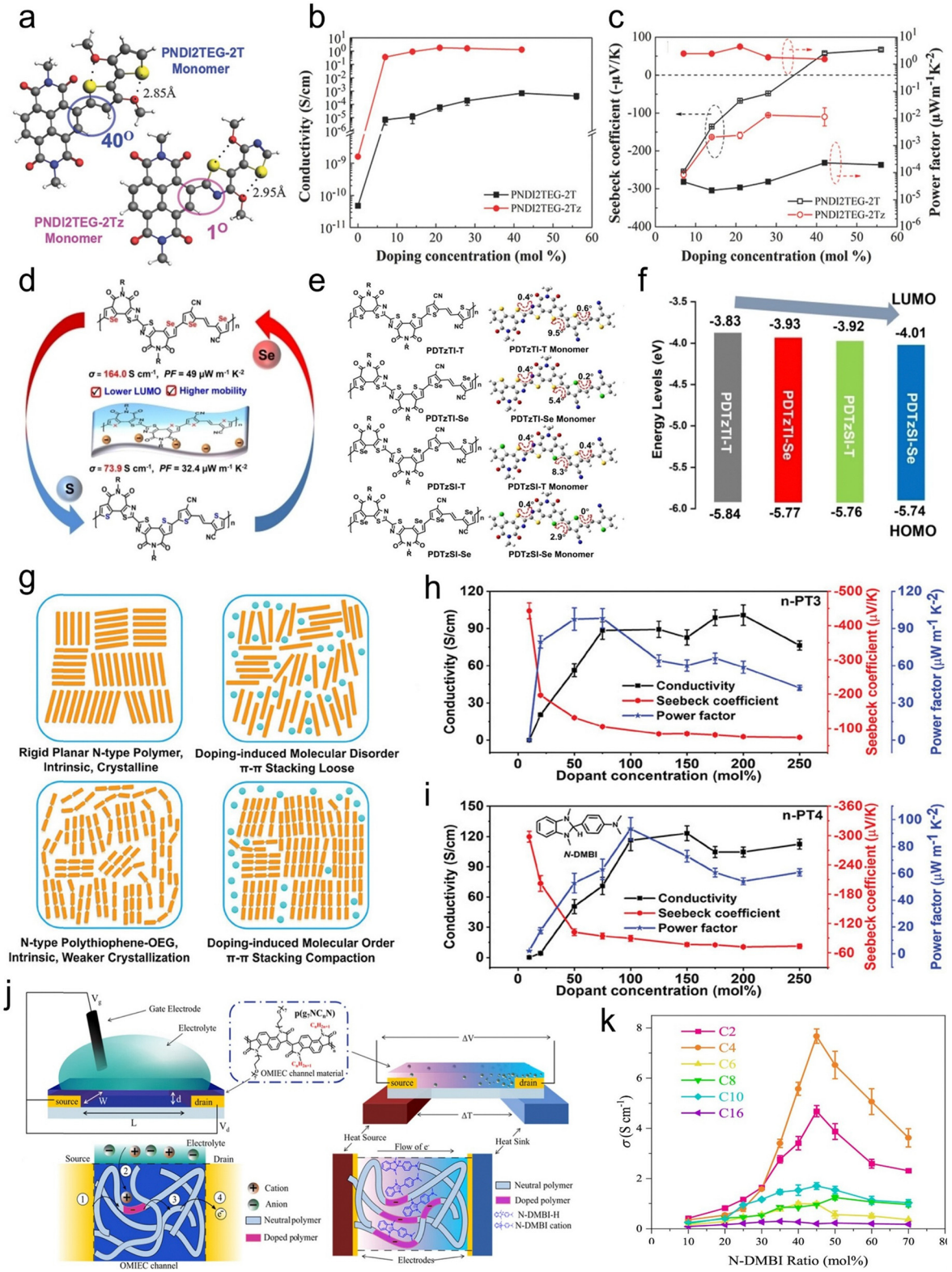

Fig. 11 (a) DFT-optimized geometries for PNDI2TEG-2T repeat unit and PNDI2TEG-2Tz repeat unit, (b) conductivity, and (c) Seebeck coefficient and power factor under various doping concentrations of doped PNDI2TEG-2T and PNDI2TEG-2Tz. Adapted with permission from ref. 35. Copyright 2018 Liu *et al.* under the terms of Creative Commons CC-BY-NC-ND license. (d) Molecular designing concept of PDTzTI-T, PDTzTI-Se, PDTzSI-T, and PDTzSI-Se. (e) Chemical structure and DFT-optimized geometries for PDTzTI-T, PDTzTI-Se, PDTzSI-T, PDTzSI-Se. (f) Energy-level alignment of PDTzTI-T, PDTzTI-Se, PDTzSI-T, PDTzSI-Se. Adapted with permission from ref. 57. Copyright 2023 Wiley-VCH GmbH. (g) Diagrammatic sketch of doping-induced molecular order, Conductivity, Seebeck coefficient, and power factor under various doping concentrations of (h) n-PT3 and (i) n-PT4. Adapted with permission from ref. 58. Copyright 2023 Wiley-VCH GmbH. (j) Molecular designing concept of p(g7NCnN)-based OMIECs. (k) Conductivity of p(g7NCnN) as a function of dopant fraction. Adapted with permission from ref. 113. Copyright 2022 American Chemical Society under the terms of the Creative Commons CC-BY license.

leading to stronger conjugation. This enhanced conjugation results in extended polaron delocalization, which improves charge carrier transport along the backbone. Moreover, the simultaneous presence of alkyl and oligo(ethylene glycol) (OEG) side chains helps balance self-assembly, aggregation, and the miscibility between dopants and hosts. Ultimately, the polymer with 75% benzene content (P-75) achieves the highest conductivity of 12 S cm^{-1} and a power factor (PF) of 13.2 μW m^{-1} K^{-2}.

Likewise, McCulloch and Marks group synthesized a series of all-acceptor fully fused polymers with mixed alkyl and OEG side chains applied as OMIECs (Fig. 11(j)).[113] They systematically adjust the content of alkyl side chains and explore the optimal ratio of alkyl side chains content and OEG side chains content. For OECT, the hydrophilic OEG side chain is beneficial for swelling, and the hydrophobic alkyl can balance the adverse effect caused by hydrated counterions. The host/dopant miscibility becomes the primary factor for OTE, significantly affecting the doping efficiency and ultimate OTE performance. Finally, the p(g_7NC_4N) achieved a maximum electrical conductivity of 7.67 S cm^{-1} and a power factor of 10.4 μW m^{-1} K^{-2} in OTE (Fig. 11(k)). This study highlighted the difference in side-chain engineering between OECT and OTE materials.

4. From molecular design to device application

Organic thermoelectric generators (OTEGs) are devices that utilize organic materials for thermoelectric conversion. To enhance the output voltage and power generation of thermoelectric generators, both p-type and n-type legs are integrated into a single device. This is achieved by connecting multiple thermoelectric legs in arrays, where the legs are electrically connected in series to increase the voltage and thermally connected in parallel to maintain a uniform temperature gradient across the device. However, significant efforts have been devoted to fabricating OTEGs using only p-type legs,[30,31,114–116] primarily due to the poor thermoelectric performance of n-type materials, which results in considerable current and power losses in p–n OTEGs. In 2021, Fabiano *et al.*[117] reported an ethanol-based n-type conductive ink (BBL:PEI) to realize high-performance p–n legs in OTEGs. After thermal activation, the ink achieved a high conductivity of 8 S cm^{-1} and demonstrated exceptional stability under ambient conditions. When combined with PEDOT:PSS, the fabricated p–n legs showed a recorded high output power of 56 nW per p–n pair at ΔT = 50 K. The BBL:PEI/PEDOT:PSS p–n legs were further used to produce a device with a high density of thermocouples,[118] demonstrating the great potential of p–n legs with balanced performance in p-type and n-type materials. While other studies focus on identifying matchable n-type legs through side-chain engineering of optimized molecules. As previously discussed, PTEG-1 exhibited good OTE performance. When used as n-type legs and combined with PEDOT:PSS p-type legs, micro-thermoelectric generators were fabricated using direct writing techniques and achieved a power density of 30.5 nW cm^{-2} at ΔT = 25 K.[119] Pei *et al.* reported a thermally activated triaminomethane-based dopant (TAM) to address challenges in n-type doping, such as poor stability and miscibility.[120] Due to its good miscibility, the dopant tends to localize in the alkyl side-chain region of the FBDPPV, thereby preserving crystallinity and achieving high thermoelectric performance. Finally, the first flexible all-polymer thermoelectric generator was fabricated by using TAM-doped FBDPPV as n-type legs and PEDOT:PSS as p-type legs, delivering a power output of 77 nW at ΔT = 46.5 K.

Air stability is a critical issue in high-performance n-type thermoelectric materials, which limits the application of n-legs in OTEGs.[121,122] Various strategies have been explored to enhance the air stability of n-type materials, including improving crystallinity,[62] lowering LUMO levels[83] and achieving *in situ* doping.[26] When designing n-type materials for thermoelectrics, air stability must be carefully considered to ensure their suitability as n-leg candidates. Some studies have suggested that incorporating OEG side chains can improve the air stability of n-type materials,[50,103] although the underlying mechanisms behind this improvement remain unexplored. In the development of air-stable n-type materials, side-chain engineering represents a promising approach. Furthermore, OTEGs operate under temperature gradients for extended periods, which necessitates high thermal stability in materials. The strong interaction between OEG side chains and dopants reduces the diffusion upon thermal stress, and thus enhances the thermal stability in both n-doped and p-doped systems.[23,123–125] Additionally, OEG side chains can bind the salt dopant through coordination and enhance thermal stability.[126] Another approach to avoid thermal diffusion of dopants is to develop all-polymer system.[127–129] These systems exhibited excellent thermal stability, which is attributed to the more difficult diffusion of polymer dopants. Here, we emphasize the importance of side chains in improving the stability under both annealing and ambient conditions, while maintaining the solution-processability and flexibility of organic thermoelectrics.

5. Conclusions and outlook

In this concise review, we explore and analyse the pivotal impact of side-chain engineering on improving the performance of n-type organic thermoelectric materials. Although the conjugated backbone plays a crucial role in determining the electronic properties of these materials, side-chain engineering allows for precise adjustments in solubility, molecular packing, and thin film morphology.

The first section of this review examines the influence of conventional alkyl side chains on molecular packing and charge transport in n-type organic thermoelectric materials. Replacing bulky, branched alkyl side chains with linear ones is a practical and straightforward approach to increasing charge mobility and doping efficiency. This enhancement is attributed to the reduced steric hindrance of linear alkyl side chains, which facilitates tighter packing of polymer chains and improves thermoelectric performance. Additionally, carefully modifying the branching point of alkyl side chains from the backbone has

significantly enhanced the thin film crystallinity, charge mobility, and electrical conductivity of these materials.

The second section reviews n-type organic thermoelectric materials featuring OEG side chains. Incorporating polar OEG side chains on n-type conjugated molecules serves a dual function: it increases the polarity of the host, preventing phase separation and improving host/dopant miscibility, thereby enhancing doping efficiency. It also raises the dielectric constant of the organic thermoelectric materials, leading to stronger electrostatic interactions between CTCs and the polar OEG side chains. As a result, this promotes higher electrical conductivities and improves overall thermoelectric performance. Amphipathic side chains, which include an alkyl segment as a spacer between the polymer backbone and an ethylene glycol-type segment, are designed to reduce Coulomb interactions between the conjugated backbone and dopant ions. This design aims to enhance the Seebeck coefficient without significantly sacrificing conductivity.

Side-chain modifications are essential to further advance the development of n-type organic thermoelectric materials. Key strategies include: (i) optimizing side chains and integrating them with innovative conjugated frameworks to create organic thermoelectric materials that exhibit high charge mobility, excellent host/dopant miscibility, and air stability. (ii) New synthetic methods are being developed to introduce a variety of functional groups into the side chains of n-type conjugated polymers specifically tailored for thermoelectric applications. A potential future direction might involve incorporating side chains with highly polarized groups, which could increase the dielectric constant and promote free charge generation, thereby enhancing the Seebeck coefficient. It is expected that continued efforts in molecular design, coupled with a deeper understanding of the molecular doping mechanism, will further advance the field of organic thermoelectric materials.

Data availability

No primary research results, software, or code have been included, and no new data were generated or analysed as part of this review. All data discussed in this review paper can be found in the original papers (references).

Conflicts of interest

There are no conflicts to declare.

Acknowledgements

The authors are grateful for the financial support from the National Natural Science Foundation of China (no. 52273201, 62105239). G. Y. also acknowledges the China Postdoctoral Science Foundation Funded Project (no. grant 2022M723077).

References

1 L. E. Bell, *Science*, 2008, **321**, 1457–1461.
2 G. J. Snyder and E. S. Toberer, *Nat. Mater.*, 2008, **7**, 105–114.
3 M. Culebras, C. M. Gómez and A. Cantarero, *Materials*, 2014, **7**, 6701–6732.
4 S. Shao and J. Liu, *CCS Chem.*, 2021, **3**, 2702–2716.
5 S. Rafique, M. R. Burton, N. Badiei, J. Gonzalez-Feijoo, S. Mehraban, M. J. Carnie, A. Tarat and L. Li, *ACS Appl. Mater. Interfaces*, 2020, **12**, 30643–30651.
6 Y.-S. Kim, H. Kim, T. Yoon, M.-J. Kim, J. Lee, H. Lee, D. Lee, Y. J. Song, J. Kwon, S. B. Jo, J. H. Cho, S. G. Lee and B. Kang, *Chem. Eng. J.*, 2023, **470**, 144129.
7 Y. Gao, Y. Ke, T. Wang, Y. Shi, C. Wang, S. Ding, Y. Wang, Y. Deng, W. Hu and Y. Geng, *Angew. Chem., Int. Ed.*, 2024, **63**, e202402642.
8 F. Huewe, A. Steeger, K. Kostova, L. Burroughs, I. Bauer, P. Strohriegl, V. Dimitrov, S. Woodward and J. Pflaum, *Adv. Mater.*, 2017, **29**, 1605682.
9 H. Wang and C. Yu, *Joule*, 2019, **3**, 53–80.
10 D. Zhou, H. Zhang, H. Zheng, Z. Xu, H. Xu, H. Guo, P. Li, Y. Tong, B. Hu and L. Chen, *Small*, 2022, **18**, 2200679.
11 T. S. Lee, S. Nam, J. G. Oh, E. H. Suh, J. Jung, H. Oh, Y. J. Jeong and J. Jang, *Chem. Eng. J.*, 2023, **455**, 140925.
12 L. Chen, X. Rong, Z. Liu, Q. Ding, X. Li, Y. Jiang, W. Han and J. Lou, *Chem. Eng. J.*, 2024, **481**, 148797.
13 X. Dai, Y. Wang, K. Li, G. Li, J. Wang, X. Sun, L. Zhang and H. Wang, *ACS Energy Lett.*, 2021, **6**, 4355–4364.
14 S. Masoumi, S. O'Shaughnessy and A. Pakdel, *Nano Energy*, 2022, **92**, 106774.
15 J. Cai and G. D. Mahan, *Phys. Rev. B: Condens. Matter Mater. Phys.*, 2006, **74**, 075201.
16 H. Fritzsche, *Solid State Commun.*, 1971, **9**, 1813–1815.
17 T. J. Seebeck, *Ann. Phys.*, 1826, **82**, 253–286.
18 G. J. Snyder and A. H. Snyder, *Energy Environ. Sci.*, 2017, **10**, 2280–2283.
19 E. Witkoske, X. Wang, J. Maassen and M. Lundstrom, *Mater. Today Phys.*, 2019, **8**, 43–48.
20 X. Wang, K. D. Parrish, J. A. Malen and P. K. L. Chan, *Sci. Rep.*, 2015, **5**, 16095.
21 M. Ma, L. Zhang, T. Yao, H. Yang, J. Liu and J. Liu, *Polym. Sci. Technol.*, 2025, DOI: **10.1021/polymscitech.5c00042**.
22 Y. Lu, J.-Y. Wang and J. Pei, *Chem. Mater.*, 2019, **31**, 6412–6423.
23 J. Liu, B. van der Zee, R. Alessandri, S. Sami, J. Dong, M. I. Nugraha, A. J. Barker, S. Rousseva, L. Qiu, X. Qiu, N. Klasen, R. C. Chiechi, D. Baran, M. Caironi, T. D. Anthopoulos, G. Portale, R. W. A. Havenith, S. J. Marrink, J. C. Hummelen and L. J. A. Koster, *Nat. Commun.*, 2020, **11**, 5694.
24 W. Zhao, J. Ding, Y. Zou, C.-a Di and D. Zhu, *Chem. Soc. Rev.*, 2020, **49**, 7210–7228.
25 F. Zhang and C.-a Di, *Chem. Mater.*, 2020, **32**, 2688–2702.
26 H. Tang, Y. Liang, C. Liu, Z. Hu, Y. Deng, H. Guo, Z. Yu, A. Song, H. Zhao, D. Zhao, Y. Zhang, X. Guo, J. Pei, Y. Ma, Y. Cao and F. Huang, *Nature*, 2022, **611**, 271–277.

27 D. Wang, J. Ding, Y. Ma, C. Xu, Z. Li, X. Zhang, Y. Zhao, Y. Zhao, Y. Di, L. Liu, X. Dai, Y. Zou, B. Kim, F. Zhang, Z. Liu, I. McCulloch, M. Lee, C. Chang, X. Yang, D. Wang, D. Zhang, L.-D. Zhao, C.-a Di and D. Zhu, *Nature*, 2024, **632**, 528–535.
28 J. Liu, L. Qiu and S. Shao, *J. Mater. Chem. C*, 2021, **9**, 16143–16163.
29 Y. Zhang, Y. Wang, C. Gao, Z. Ni, X. Zhang, W. Hu and H. Dong, *Chem. Soc. Rev.*, 2023, **52**, 1331–1381.
30 C. Wang, K. Sun, J. Fu, R. Chen, M. Li, Z. Zang, X. Liu, B. Li, H. Gong and J. Ouyang, *Adv. Sustainable Syst.*, 2018, **2**, 1800085.
31 S. Xu, M. Hong, X.-L. Shi, Y. Wang, L. Ge, Y. Bai, L. Wang, M. Dargusch, J. Zou and Z.-G. Chen, *Chem. Mater.*, 2019, **31**, 5238–5244.
32 Y.-Y. Deng, X.-L. Shi, T. Wu, H. Wu, Y.-M. Liu, M. Zhu, W.-D. Liu, M. Li, P. Huang, Q. Liu and Z.-G. Chen, *Chem. Eng. J.*, 2024, **502**, 158104.
33 Y.-Y. Deng, X.-L. Shi, T. Wu, Y. Yue, W.-D. Liu, M. Li, F. Yue, P. Huang, Q. Liu and Z.-G. Chen, *Adv. Fiber Mater.*, 2024, **6**, 1616–1628.
34 W. Yang, K. Feng, S. Ma, B. Liu, Y. Wang, R. Ding, S. Y. Jeong, H. Y. Woo, P. K. L. Chan and X. Guo, *Adv. Mater.*, 2024, **36**, 2305416.
35 J. Liu, G. Ye, B. v d Zee, J. Dong, X. Qiu, Y. Liu, G. Portale, R. C. Chiechi and L. J. A. Koster, *Adv. Mater.*, 2018, (30), 1804290.
36 Y. Lu, Z.-D. Yu, R.-Z. Zhang, Z.-F. Yao, H.-Y. You, L. Jiang, H.-I. Un, B.-W. Dong, M. Xiong, J.-Y. Wang and J. Pei, *Angew. Chem., Int. Ed.*, 2019, **58**, 11390–11394.
37 B. D. Naab, X. Gu, T. Kurosawa, J. W. F. To, A. Salleo and Z. Bao, *Adv. Electron. Mater.*, 2016, **2**, 1600004.
38 S. Wang, H. Sun, U. Ail, M. Vagin, P. O. Å. Persson, J. W. Andreasen, W. Thiel, M. Berggren, X. Crispin, D. Fazzi and S. Fabiano, *Adv. Mater.*, 2016, **28**, 10764–10771.
39 H. Li, J. Song, J. Xiao, L. Wu, H. E. Katz and L. Chen, *Adv. Funct. Mater.*, 2020, **30**, 2004378.
40 C. Dong, B. Meng, J. Liu and L. Wang, *ACS Appl. Mater. Interfaces*, 2020, **12**, 10428–10433.
41 T. Lei, J.-Y. Wang and J. Pei, *Chem. Mater.*, 2014, **26**, 594–603.
42 J. Liu, L. Qiu, G. Portale, M. Koopmans, G. ten Brink, J. C. Hummelen and L. J. A. Koster, *Adv. Mater.*, 2017, **29**, 1701641.
43 V. Vijayakumar, E. Zaborova, L. Biniek, H. Zeng, L. Herrmann, A. Carvalho, O. Boyron, N. Leclerc and M. Brinkmann, *ACS Appl. Mater. Interfaces*, 2019, **11**, 4942–4953.
44 C.-K. Mai, R. A. Schlitz, G. M. Su, D. Spitzer, X. Wang, S. L. Fronk, D. G. Cahill, M. L. Chabinyc and G. C. Bazan, *J. Am. Chem. Soc.*, 2014, **136**, 13478–13481.
45 Y. Wang, M. Nakano, T. Michinobu, Y. Kiyota, T. Mori and K. Takimiya, *Macromolecules*, 2017, **50**, 857–864.
46 Y. Wang and K. Takimiya, *Adv. Mater.*, 2020, **32**, 2002060.
47 Y. Song, J. Ding, X. Dai, C. Li, C.-a Di and D. Zhang, *ACS Mater. Lett.*, 2022, **4**, 521–527.
48 Z.-D. Yu, Y. Lu, Z.-F. Yao, H.-T. Wu, Z.-Y. Wang, C.-K. Pan, J.-Y. Wang and J. Pei, *Angew. Chem., Int. Ed.*, 2024, **63**, e202405139.
49 J. Liu, L. Qiu, R. Alessandri, X. Qiu, G. Portale, J. Dong, W. Talsma, G. Ye, A. A. Sengrian, P. C. T. Souza, M. A. Loi, R. C. Chiechi, S. J. Marrink, J. C. Hummelen and L. J. A. Koster, *Adv. Mater.*, 2018, **30**, 1704630.
50 J. Liu, L. Qiu, G. Portale, S. Torabi, M. C. A. Stuart, X. Qiu, M. Koopmans, R. C. Chiechi, J. C. Hummelen and L. J. Anton Koster, *Nano Energy*, 2018, **52**, 183–191.
51 K. Feng, J. Wang, S. Y. Jeong, W. Yang, J. Li, H. Y. Woo and X. Guo, *Adv. Sci.*, 2023, **10**, 2302629.
52 X. Yang, G. Ye, K. Tran, Y. Liu, J. Cao, J. Dong, G. Portale, J. Liu, P. Zhang, M. A. Loi, R. C. Chiechi and L. J. A. Koster, *ACS Mater. Lett.*, 2024, **6**, 1207–1215.
53 J. Liu, G. Ye, H. G. O. Potgieser, M. Koopmans, S. Sami, M. I. Nugraha, D. R. Villalva, H. Sun, J. Dong, X. Yang, X. Qiu, C. Yao, G. Portale, S. Fabiano, T. D. Anthopoulos, D. Baran, R. W. A. Havenith, R. C. Chiechi and L. J. A. Koster, *Adv. Mater.*, 2021, **33**, 2006694.
54 X. Peng, G. Ye, L. Zhang, Y. Kuang, S. Shao and J. Liu, *Macromolecules*, 2024, **57**, 7156–7164.
55 Y. Shi, J. Li, H. Sun, Y. Li, Y. Wang, Z. Wu, S. Y. Jeong, H. Y. Woo, S. Fabiano and X. Guo, *Angew. Chem., Int. Ed.*, 2022, **61**, e202214192.
56 J. Li, M. Liu, K. Yang, Y. Wang, J. Wang, Z. Chen, K. Feng, D. Wang, J. Zhang, Y. Li, H. Guo, Z. Wei and X. Guo, *Adv. Funct. Mater.*, 2023, **33**, 2213911.
57 Y. Li, W. Wu, Y. Wang, E. Huang, S. Y. Jeong, H. Y. Woo, X. Guo and K. Feng, *Angew. Chem., Int. Ed.*, 2024, **63**, e202316214.
58 S. Deng, Y. Kuang, L. Liu, X. Liu, J. Liu, J. Li, B. Meng, C.-a Di, J. Hu and J. Liu, *Adv. Mater.*, 2024, **36**, 2309679.
59 M. Alsufyani, M.-A. Stoeckel, X. Chen, K. Thorley, R. K. Hallani, Y. Puttisong, X. Ji, D. Meli, B. D. Paulsen, J. Strzalka, K. Regeta, C. Combe, H. Chen, J. Tian, J. Rivnay, S. Fabiano and I. McCulloch, *Angew. Chem., Int. Ed.*, 2022, **61**, e202113078.
60 S. D. Kang and G. J. Snyder, *Nat. Mater.*, 2017, **16**, 252–257.
61 A. M. Glaudell, J. E. Cochran, S. N. Patel and M. L. Chabinyc, *Adv. Energy Mater.*, 2015, **5**, 1401072.
62 X. Yan, M. Xiong, J.-T. Li, S. Zhang, Z. Ahmad, Y. Lu, Z.-Y. Wang, Z.-F. Yao, J.-Y. Wang, X. Gu and T. Lei, *J. Am. Chem. Soc.*, 2019, **141**, 20215–20221.
63 H.-I. Un, S. A. Gregory, S. K. Mohapatra, M. Xiong, E. Longhi, Y. Lu, S. Rigin, S. Jhulki, C.-Y. Yang, T. V. Timofeeva, J.-Y. Wang, S. K. Yee, S. Barlow, S. R. Marder and J. Pei, *Adv. Energy Mater.*, 2019, **9**, 1900817.
64 S. Guchait, S. Oummouch, P. Durand, N. Kamatham, B. Jismy, L. Herrmann, S. Mery, N. Leclerc and M. Brinkmann, *Small*, 2025, **21**, 2410073.
65 E. M. Thomas, B. C. Popere, H. Fang, M. L. Chabinyc and R. A. Segalman, *Chem. Mater.*, 2018, **30**, 2965–2972.
66 I. E. Jacobs and A. J. Moulé, *Adv. Mater.*, 2017, **29**, 1703063.
67 A. D. Scaccabarozzi, A. Basu, F. Aniés, J. Liu, O. Zapata-Arteaga, R. Warren, Y. Firdaus, M. I. Nugraha, Y. Lin,

M. Campoy-Quiles, N. Koch, C. Müller, L. Tsetseris, M. Heeney and T. D. Anthopoulos, *Chem. Rev.*, 2022, **122**, 4420–4492.
68 D. Scheunemann, E. Järsvall, J. Liu, D. Beretta, S. Fabiano, M. Caironi, M. Kemerink and C. Müller, *Chem. Phys. Rev.*, 2022, **3**, 021309.
69 P. Pingel, R. Schwarzl and D. Neher, *Appl. Phys. Lett.*, 2012, **100**, 143303.
70 H. Méndez, G. Heimel, S. Winkler, J. Frisch, A. Opitz, K. Sauer, B. Wegner, M. Oehzelt, C. Röthel, S. Duhm, D. Többens, N. Koch and I. Salzmann, *Nat. Commun.*, 2015, **6**, 8560.
71 V. I. Arkhipov, E. V. Emelianova, P. Heremans and H. Bässler, *Phys. Rev. B: Condens. Matter Mater. Phys.*, 2005, **72**, 235202.
72 S. Olthof, S. Mehraeen, S. K. Mohapatra, S. Barlow, V. Coropceanu, J.-L. Brédas, S. R. Marder and A. Kahn, *Phys. Rev. Lett.*, 2012, **109**, 176601.
73 X. Yang, G. Ye, J. Liu, R. C. Chiechi and L. J. A. Koster, *Adv. Mater.*, 2024, **36**, 2404397.
74 M. Koopmans, M. A. T. Leiviskä, J. Liu, J. Dong, L. Qiu, J. C. Hummelen, G. Portale, M. C. Heiber and L. J. A. Koster, *ACS Appl. Mater. Interfaces*, 2020, **12**, 56222–56230.
75 I. E. Jacobs, G. D'Avino, V. Lemaur, Y. Lin, Y. Huang, C. Chen, T. F. Harrelson, W. Wood, L. J. Spalek, T. Mustafa, C. A. O'Keefe, X. Ren, D. Simatos, D. Tjhe, M. Statz, J. W. Strzalka, J.-K. Lee, I. McCulloch, S. Fratini, D. Beljonne and H. Sirringhaus, *J. Am. Chem. Soc.*, 2022, **144**, 3005–3019.
76 R. A. Schlitz, F. G. Brunetti, A. M. Glaudell, P. L. Miller, M. A. Brady, C. J. Takacs, C. J. Hawker and M. L. Chabinyc, *Adv. Mater.*, 2014, **26**, 2825–2830.
77 C. J. Boyle, M. Upadhyaya, P. Wang, L. A. Renna, M. Lu-Díaz, S. Pyo Jeong, N. Hight-Huf, L. Korugic-Karasz, M. D. Barnes, Z. Aksamija and D. Venkataraman, *Nat. Commun.*, 2019, **10**, 2827.
78 Y. Lu, Z.-D. Yu, H.-I. Un, Z.-F. Yao, H.-Y. You, W. Jin, L. Li, Z.-Y. Wang, B.-W. Dong, S. Barlow, E. Longhi, C.-a Di, D. Zhu, J.-Y. Wang, C. Silva, S. R. Marder and J. Pei, *Adv. Mater.*, 2021, **33**, 2005946.
79 E. E. Perry, C.-Y. Chiu, K. Moudgil, R. A. Schlitz, C. J. Takacs, K. A. O'Hara, J. G. Labram, A. M. Glaudell, J. B. Sherman, S. Barlow, C. J. Hawker, S. R. Marder and M. L. Chabinyc, *Chem. Mater.*, 2017, **29**, 9742–9750.
80 Y. Shin, M. Massetti, H. Komber, T. Biskup, D. Nava, G. Lanzani, M. Caironi and M. Sommer, *Adv. Electron. Mater.*, 2018, **4**, 1700581.
81 J. H. Burke and M. J. Bird, *Adv. Mater.*, 2019, **31**, 1806863.
82 B. Lüssem, M. Riede and K. Leo, *Phys. Status Solidi A*, 2013, **210**, 9–43.
83 D. Nava, Y. Shin, M. Massetti, X. Jiao, T. Biskup, M. S. Jagadeesh, A. Calloni, L. Duò, G. Lanzani, C. R. McNeill, M. Sommer and M. Caironi, *ACS Appl. Energy Mater.*, 2018, **1**, 4626–4634.
84 S. Wang, H. Sun, T. Erdmann, G. Wang, D. Fazzi, U. Lappan, Y. Puttisong, Z. Chen, M. Berggren, X. Crispin, A. Kiriy, B. Voit, T. J. Marks, S. Fabiano and A. Facchetti, *Adv. Mater.*, 2018, **30**, 1801898.
85 K. Shi, F. Zhang, C.-a Di, T.-W. Yan, Y. Zou, X. Zhou, D. Zhu, J.-Y. Wang and J. Pei, *J. Am. Chem. Soc.*, 2015, **137**, 6979–6982.
86 Y. Zeng, W. Zheng, Y. Guo, G. Han and Y. Yi, *J. Mater. Chem. A*, 2020, **8**, 8323–8328.
87 R. Ghosh, A. R. Chew, J. Onorato, V. Pakhnyuk, C. K. Luscombe, A. Salleo and F. C. Spano, *J. Phys. Chem. C*, 2018, **122**, 18048–18060.
88 D. Kiefer, R. Kroon, A. I. Hofmann, H. Sun, X. Liu, A. Giovannitti, D. Stegerer, A. Cano, J. Hynynen, L. Yu, Y. Zhang, D. Nai, T. F. Harrelson, M. Sommer, A. J. Moulé, M. Kemerink, S. R. Marder, I. McCulloch, M. Fahlman, S. Fabiano and C. Müller, *Nat. Mater.*, 2019, **18**, 149–155.
89 H. Chen, M. Moser, S. Wang, C. Jellett, K. Thorley, G. T. Harrison, X. Jiao, M. Xiao, B. Purushothaman, M. Alsufyani, H. Bristow, S. De Wolf, N. Gasparini, A. Wadsworth, C. R. McNeill, H. Sirringhaus, S. Fabiano and I. McCulloch, *J. Am. Chem. Soc.*, 2021, **143**, 260–268.
90 J. Liu, Y. Shi, J. Dong, M. I. Nugraha, X. Qiu, M. Su, R. C. Chiechi, D. Baran, G. Portale, X. Guo and L. J. A. Koster, *ACS Energy Lett.*, 2019, **4**, 1556–1564.
91 T. J. Aubry, K. J. Winchell, C. Z. Salamat, V. M. Basile, J. R. Lindemuth, J. M. Stauber, J. C. Axtell, R. M. Kubena, M. D. Phan, M. J. Bird, A. M. Spokoyny, S. H. Tolbert and B. J. Schwartz, *Adv. Funct. Mater.*, 2020, **30**, 2001800.
92 S. Wang, D. Fazzi, Y. Puttisong, M. J. Jafari, Z. Chen, T. Ederth, J. W. Andreasen, W. M. Chen, A. Facchetti and S. Fabiano, *Chem. Mater.*, 2019, **31**, 3395–3406.
93 A. Facchetti, *Chem. Mater.*, 2011, **23**, 733–758.
94 A. Uva, A. Lin and H. Tran, *J. Am. Chem. Soc.*, 2023, **145**, 3606–3614.
95 J. Zhao, X. Huang, Q. Li, S. Liu, Z. Fan, D. Zhang, S. Ma, Z. Cao, X. Jiao, Y.-P. Cai and F. Huang, *J. Energy Chem.*, 2021, **53**, 69–76.
96 J. Li, K. Yang, D. Wang, B. Liu, Y. Wang, S. Y. Jeong, Z. Chen, H. Y. Woo and X. Guo, *Macromolecules*, 2023, **56**, 2339–2347.
97 X. Tang, Y. Wu, G. He, J. Wu, F. Zhong, Z. Ren, G. Cao, F. Liu, C. Gao and L. Wang, *Chem. Eng. J.*, 2024, **495**, 153358.
98 Q.-Y. Li, Z.-F. Yao, H.-T. Wu, L. Luo, Y.-F. Ding, C.-Y. Yang, X.-Y. Wang, Z. Shen, J.-Y. Wang and J. Pei, *Angew. Chem., Int. Ed.*, 2022, **61**, e202200221.
99 K. O'Hara, C. J. Takacs, S. Liu, F. Cruciani, P. Beaujuge, C. J. Hawker and M. L. Chabinyc, *Macromolecules*, 2019, **52**, 2853–2862.
100 E. M. Thomas, E. C. Davidson, R. Katsumata, R. A. Segalman and M. L. Chabinyc, *ACS Macro Lett.*, 2018, **7**, 1492–1497.
101 L. Qiu, J. Liu, R. Alessandri, X. Qiu, M. Koopmans, R. W. A. Havenith, S. J. Marrink, R. C. Chiechi, L. J. Anton Koster and J. C. Hummelen, *J. Mater. Chem. A*, 2017, **5**, 21234–21241.
102 S. Gámez-Valenzuela, J. Li, S. Ma, S. Y. Jeong, H. Y. Woo, K. Feng and X. Guo, *Angew. Chem., Int. Ed.*, 2024, **63**, e202408537.

103 D. Kiefer, A. Giovannitti, H. Sun, T. Biskup, A. Hofmann, M. Koopmans, C. Cendra, S. Weber, L. J. Anton Koster, E. Olsson, J. Rivnay, S. Fabiano, I. McCulloch and C. Müller, *ACS Energy Lett.*, 2018, **3**, 278–285.

104 Y.-h Shin, H. Komber, D. Caiola, M. Cassinelli, H. Sun, D. Stegerer, M. Schreiter, K. Horatz, F. Lissel, X. Jiao, C. R. McNeill, S. Cimò, C. Bertarelli, S. Fabiano, M. Caironi and M. Sommer, *Macromolecules*, 2020, **53**, 5158–5168.

105 J. Liu, S. Maity, N. Roosloot, X. Qiu, L. Qiu, R. C. Chiechi, J. C. Hummelen, E. von Hauff and L. J. A. Koster, *Adv. Electron. Mater.*, 2019, **5**, 1800959.

106 A. I. Hochbaum, R. Chen, R. D. Delgado, W. Liang, E. C. Garnett, M. Najarian, A. Majumdar and P. Yang, *Nature*, 2008, **451**, 163–167.

107 M. Beekman, D. T. Morelli and G. S. Nolas, *Nat. Mater.*, 2015, **14**, 1182–1185.

108 K. N. Baustert, J. H. Bombile, M. T. Rahman, A. O. Yusuf, R. Li, A. J. Huckaba, C. Risko and K. R. Graham, *Adv. Mater.*, 2024, **36**, 2313863.

109 M. Koopmans and L. J. A. Koster, *Appl. Phys. Lett.*, 2021, **119**, 143301.

110 Z.-D. Yu, Y. Lu, Z.-Y. Wang, H.-I. Un, S. J. Zelewski, Y. Cui, H.-Y. You, Y. Liu, K.-F. Xie, Z.-F. Yao, Y.-C. He, J.-Y. Wang, W.-B. Hu, H. Sirringhaus and J. Pei, *Sci. Adv.*, 2023, **9**, eadf3495.

111 J. Han, A. Chiu, C. Ganley, P. McGuiggan, S. M. Thon, P. Clancy and H. E. Katz, *Angew. Chem., Int. Ed.*, 2021, **60**, 27212–27219.

112 C. Dong, S. Deng, B. Meng, J. Liu and L. Wang, *Angew. Chem., Int. Ed.*, 2021, **60**, 16184–16190.

113 A. Marks, X. Chen, R. Wu, R. B. Rashid, W. Jin, B. D. Paulsen, M. Moser, X. Ji, S. Griggs, D. Meli, X. Wu, H. Bristow, J. Strzalka, N. Gasparini, G. Costantini, S. Fabiano, J. Rivnay and I. McCulloch, *J. Am. Chem. Soc.*, 2022, **144**, 4642–4656.

114 N. Kim, S. Lienemann, I. Petsagkourakis, D. Alemu Mengistie, S. Kee, T. Ederth, V. Gueskine, P. Leclère, R. Lazzaroni, X. Crispin and K. Tybrandt, *Nat. Commun.*, 2020, **11**, 1424.

115 E. Jin Bae, Y. Hun Kang, K.-S. Jang and S. Yun Cho, *Sci. Rep.*, 2016, **6**, 18805.

116 S. Hwang, W. J. Potscavage, R. Nakamichi and C. Adachi, *Org. Electron.*, 2016, **31**, 31–40.

117 C.-Y. Yang, M.-A. Stoeckel, T.-P. Ruoko, H.-Y. Wu, X. Liu, N. B. Kolhe, Z. Wu, Y. Puttisong, C. Musumeci, M. Massetti, H. Sun, K. Xu, D. Tu, W. M. Chen, H. Y. Woo, M. Fahlman, S. A. Jenekhe, M. Berggren and S. Fabiano, *Nat. Commun.*, 2021, **12**, 2354.

118 N. J. Pataki, N. Zahabi, Q. Li, P. Rossi, M. Cassinelli, M. Butti, M. Massetti, S. Fabiano, I. Zozoulenko and M. Caironi, *Adv. Funct. Mater.*, 2024, **34**, 2400982.

119 M. Massetti, S. Bonfadini, D. Nava, M. Butti, L. Criante, G. Lanzani, L. Qiu, J. C. Hummelen, J. Liu, L. J. A. Koster and M. Caironi, *Nano Energy*, 2020, **75**, 104983.

120 C.-Y. Yang, Y.-F. Ding, D. Huang, J. Wang, Z.-F. Yao, C.-X. Huang, Y. Lu, H.-I. Un, F.-D. Zhuang, J.-H. Dou, C.-a Di, D. Zhu, J.-Y. Wang, T. Lei and J. Pei, *Nat. Commun.*, 2020, **11**, 3292.

121 L. M. Cowen, J. Atoyo, M. J. Carnie, D. Baran and B. C. Schroeder, *ECS J. Solid State Sci. Technol.*, 2017, **6**, N3080.

122 D. Yuan, W. Liu and X. Zhu, *Chem. Soc. Rev.*, 2023, **52**, 3842–3872.

123 B. X. Dong, C. Nowak, J. W. Onorato, T. Ma, J. Niklas, O. G. Poluektov, G. Grocke, M. F. DiTusa, F. A. Escobedo, C. K. Luscombe, P. F. Nealey and S. N. Patel, *Chem. Mater.*, 2021, **33**, 741–753.

124 R. Kroon, D. Kiefer, D. Stegerer, L. Yu, M. Sommer and C. Müller, *Adv. Mater.*, 2017, **29**, 1700930.

125 J. Li, C. W. Rochester, I. E. Jacobs, E. W. Aasen, S. Friedrich, P. Stroeve and A. J. Moulé, *Org. Electron.*, 2016, **33**, 23–31.

126 J. Liu, M. P. Garman, J. Dong, B. van der Zee, L. Qiu, G. Portale, J. C. Hummelen and L. J. A. Koster, *ACS Appl. Energy Mater.*, 2019, **2**, 6664–6671.

127 K. Xu, H. Sun, T.-P. Ruoko, G. Wang, R. Kroon, N. B. Kolhe, Y. Puttisong, X. Liu, D. Fazzi, K. Shibata, C.-Y. Yang, N. Sun, G. Persson, A. B. Yankovich, E. Olsson, H. Yoshida, W. M. Chen, M. Fahlman, M. Kemerink, S. A. Jenekhe, C. Müller, M. Berggren and S. Fabiano, *Nat. Mater.*, 2020, **19**, 738–744.

128 J. Han, E. Tiernan, T. Lee, A. Chiu, P. McGuiggan, N. Adams, J. A. Tomko, P. E. Hopkins, S. M. Thon, J. D. Tovar and H. E. Katz, *Adv. Mater.*, 2022, **34**, 2201062.

129 X. Fan, J. Liu, X. Duan, H. Li, S. Deng, Y. Kuang, J. Li, C. Lin, B. Meng, J. Hu, S. Wang, J. Liu and L. Wang, *Adv. Sci.*, 2024, **11**, 2401952.